UNIVERSITY OF TROMSØ UIT

FACULTY OF SCIENCE AND TECHNOLOGY
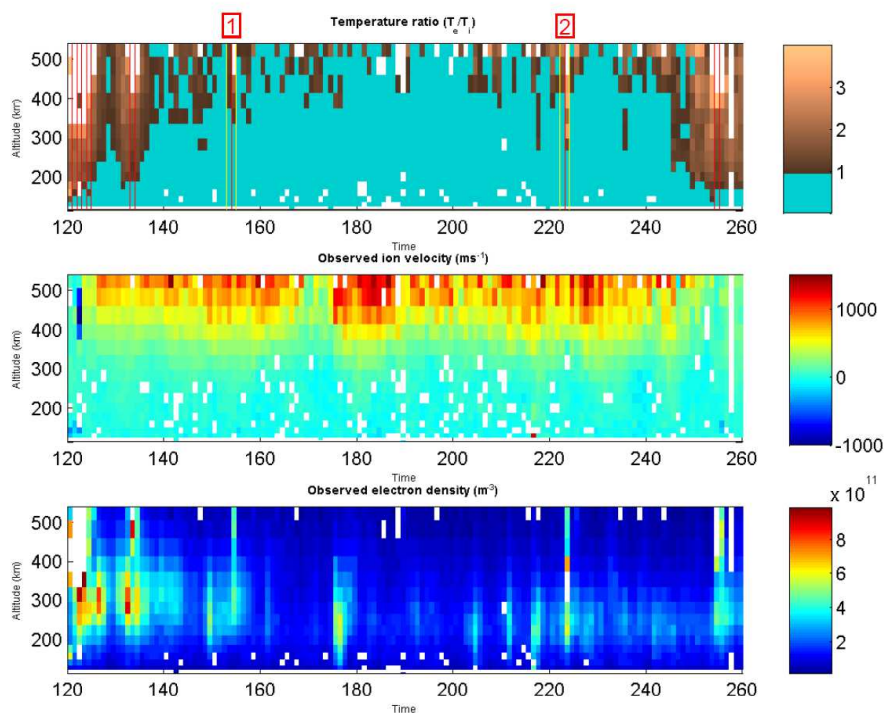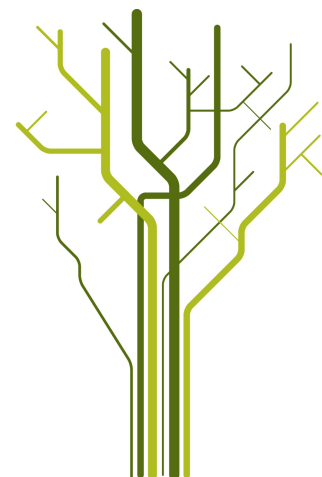DEPARTMENT OF PHYSICS AND TECHNOLOGY

Type-I ion outflow from the high latitude ionosphere

Chiara Argese

FYS-3900 Master's Thesis in Space Physics

December 2013

"Learn from yesterday, live for today, hope for tomorrow.
The important thing is to not stop questioning."
(Albert Einstein)

Contents

Abstract

The aim of this thesis is to study the type-I ion outflows in the high latitude ionosphere. Type-I ion outflows are characterized by the presence of strong perpendicular electric fields, enhanced and anisotropic ion temperatures and low electron densities below 300 km, indicating small amounts of hard particle precipitation.

We scanned data from the EISCAT Madrigal database over a period of 10 years (January 2000 - December 2010). In order to detect type-I ion outflows we checked the colour plots of the field-aligned experiments ran with the UHF, the VHF and the ESR radars. Data from the type-I candidates have then been analyzed using a matlab program which plots the temperature ratio T_e/T_i as a function of both time and altitude.

Type-I ion outflows have been divided into two categories: non-continuous and continuous outflows, depending on the profile of the temperature ratio. Continuous outflows have been detected with the ESR (EISCAT Svalbard Radar) and only at high altitudes (> 400 km) with the VHF radar. As a consequence, we suggest different ion heating mechanisms at different locations and altitudes. Furthermore, type-I ion outflows have been detected only in the evening sector with the UHF and VHF radars, but both in the morning and evening sectors with the ESR radars, suggesting that particle precipitations may be of relevance to trigger these outflows.
A third type of ion outflows has been identified showing a fast changing temperature ratio profile .

When possible we checked the presence of naturally enhanced ion acoustic lines (NEIALs) during type-I ion outflows. Few data were available, the real-time-graph programs from EISCAT were available for 4 outflow events. We found NEIALs during 1 outflow event detected with the ESR radar, suggesting that the proposed theories in the literature about the NEIAL generation mechanisms should be discussed in the future or other mechanisms are needed to fulfill the requirement of a temperature ratio less than 1.

1. Introduction

The ionosphere is the region of the atmosphere where significant numbers of free thermal electrons and ions are present. The free electrons and ions are produced via ionization of the neutral particles both by extreme ultraviolet radiation from the Sun and by collisions with energetic particles that penetrate the atmosphere (*Schunk and Nagy* (2009)). Once the charged particles are formed they are affected by many different physical processes.

In order to understand these processes an understanding of several topics is required, this is the reason why in the second chapter we give a brief overview of the Sun and its magnetic field first and of the Earth and its atmosphere secondly.

It has already been established that the ionosphere is a significant source of plasma for the magnetosphere (*Nishida* (1966)). The phenomenon of the outflow has been extensively studied in the last years, they have been divided into two main categories: type-I ion outflows where the ion temperature is enhanced and type-II ion outflows where the electron temperature is enhanced. The aim of this thesis is to identify and study type-I ion outflows. An overview about type-I ion outflows, their acceleration and heating mechanisms is given in the second chapter.

We used data from the three incoherent scatter radars UHF, VHF and ESR operated by EISCAT. In the third chapter we give an overview about the EISCAT system and the incoherent scatter technique. Amongst the various parameters obtained by the radars, in order to detect type-I ion outflows we were interested in analyzing the electron density profile, together with the electron and ion temperatures and the ion drift velocity. We identified type-I ion outflows over a 10 year time interval (2000-2010).

Literature about type-II ion outflows associated with NEIALs is abundant, but a study about the possible association between type-I ion outflows and NEIALs is still lacking. We verified, when possible, if NEIALs were present during type-I ion outflows. In chapter 4 we present the observations and results obtained.

In the fifth chapter a discussion is given. Conclusion and ideas about possible future works are given in the sixth chapter.

2. Background

In this chapter we give an introduction about the Sun and the Earth. In the first section we describe the Sun and its main characteristics; in the second section we describe the magnetic field of the Earth; an overview of the atmosphere of the Earth is given and then we discuss more in detail the Earth's ionosphere. Next follows a description of ion outflows and what are believed to be the main acceleration and heating mechanisms. In the last section we describe the naturally enhanced ion acoustic lines and their more accredited generation mechanisms.

2.1. The Sun

2.1.1. General about the Sun

The Sun is a star of average mass $m_S \simeq 1.99 \times 10^{30} kg$, radius $r_S \simeq 6.96 \times 10^8 m$ and luminosity $L_S \simeq 3.84 \times 10^{26} Watts$. Chemically the Sun is mainly composed of hydrogen and helium with small amounts of heavier elements, including oxygen, carbon and iron among the others.

The energy of the Sun is generated by the nuclear fusion of the hydrogen into helium in the very hot central core, this energy then arrives to the convective zone through the radiative zone (see Fig. 2.1). Due to the strong convection in the outer zone the solar surface is irregular displaying both small-scale and large-scale convective cells or granules (*Schunk and Nagy* (2009)).

The Sun's atmosphere is composed of two regions: the photosphere and the chromosphere. The corona extends much further outside the actual atmosphere of the Sun. The photosphere is the innermost region and is where the visible radiation comes from; the temperature of this layer decreases with radial distance from about 8000 K at its sunward boundary to about 4500 K near the photosphere-chromosphere boundary. In the chromosphere, which is a layer thick $\sim 500 km$, the temperature increases from the minimum of 4500 K to about 6000 K close to the base of the corona, this is the hottest region ($\sim 10^6 K$) which contains ionized plasma that extends several radii from the Sun (*Karttunen et al.* (2007)).

2.1.2. The solar magnetic field

Close to the Sun the solar magnetic field is basically dipolar. In these closed field lines the hot plasma can be trapped. Away from the Sun, the high coronal temperatures cause
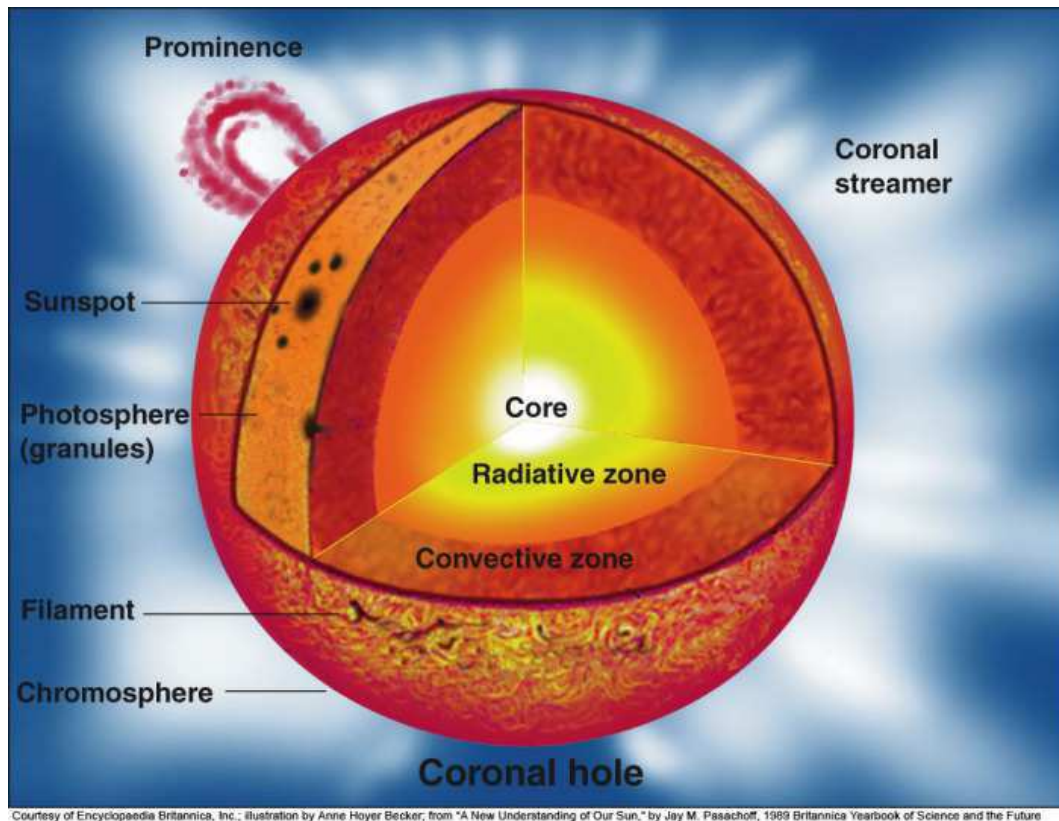
Figure 2.1.: Schematic illustration of the Sun interior (Figure from http://www.ifa.hawaii.edu/~barnes/ast110_06/tsaas.html).

a continuous outflow of plasma from the corona, the so called solar wind. As this hot plasma flows radially away from the Sun, it tends to drag the dipolar magnetic field lines with it into interplanetary space (see Fig. 2.2). Hot coronal plasma can be trapped on strong magnetic field loops, but depending on the strength of the magnetic field some hot plasma can slowly escape from these loops, forming coronal streamers that extend into space and are the source of the slow component of the solar wind. However, the hot plasma can easily escape from the corona where the Sun's magnetic field does not loop, but extends in the radial direction. This is the source of the high-speed component of the solar wind (*Schunk and Nagy* (2009)).

The Sun rotates with a period of about 27 days, but there is a differential rotation between the equator (25 days) and the poles (31 days) due to the fact that the Sun's surface is not solid. The main consequence of this rotation and plasma convection is the production of intense electric currents and magnetic fields via a dynamo action. The magnetic fields that are generated display a distinct temporal variation. Specifically, the magnetic activity increases and decreases following a 22-year cycle, which coincides with the change in polarity of the Sun's magnetic poles (*Schunk and Nagy* (2009)). One of the primary phenomenon related to the solar magnetic activity is the appearance of sunspots, which are dark regions that can last from several hours to several months. The reason why the sunspots are dark areas is that they are cooler areas than the surroundings (a sunspot has typically temperatures of $\sim 1500K$ below that of its surroundings) due to intense localized
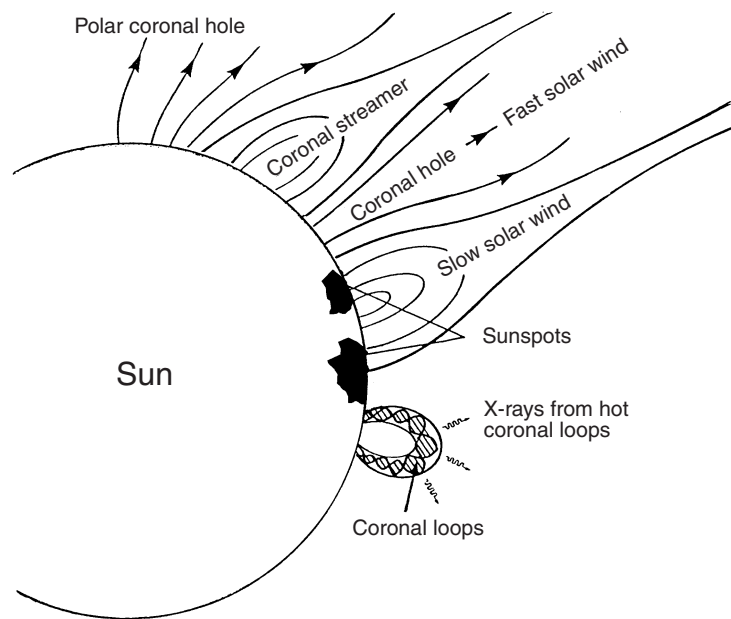
Figure 2.2.: Illustration of the magnetic field in the corona and coronal features (Figure from *Schunk and Nagy* (2009)).

magnetic fields which inhibit convection.

Other features of the solar activity are flares, which are the most violent form of solar activity. The flares send bursts of energetic particles into space, releasing a large amount of energy stored in the magnetic field. Another type of explosion stems from prominences, which extend far in the Sun's atmosphere and follow the loop of closed magnetic flux tubes. Sometimes eruptive prominences occur, the flux tubes break and gas is violently thrown into space (*Karttunen et al.* (2007)).

2.1.3. The interplanetary magnetic field

As the solar wind expands into space it increases its velocity and at a distance of a few solar radii it becomes supersonic (the Mach number is greater than 1). At about the same distance the rarefied solar wind plasma becomes collisionless (the collisional mean free path exceeds the characteristic scale length for density changes). In a collisionless plasma electric currents flow with little resistance resulting in the fact that the solar magnetic field gets frozen into the solar wind and is carried out into space with it, becoming what is known as the interplanetary magnetic field (hereafter IMF).

The Sun rotation acts to bend the magnetic field lines drawn outward by the radial solar wind forming spirals. The well known ballerina skirt model describes these spirals in three dimensions (see Fig. 2.3) (*Schunk and Nagy* (2009)).
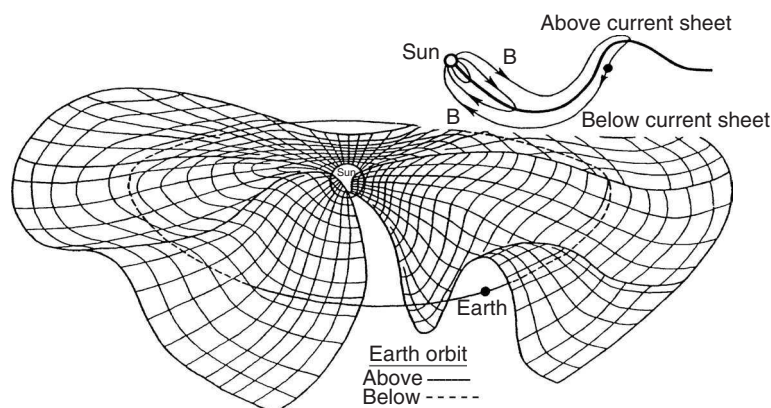
Figure 2.3.: Three-dimensional sketch of the current sheet that flows in an azimuthal direction around the Sun. At the top of the figure it's possible to see the opposite polarities of the magnetic fields on the two sides of the current sheet (Figure from *Schunk and Nagy* (2009)).

2.2. The Earth

2.2.1. The magnetic field

The Earth's magnetic field is closely approximated by the magnetic field of a dipole whose axis is tilted with respect to the spin axis of the Earth by about 11°. In the Northern hemisphere the magnetic field points toward the surface of the Earth, while in the Southern hemisphere it points away from it, see Fig. 2.4.
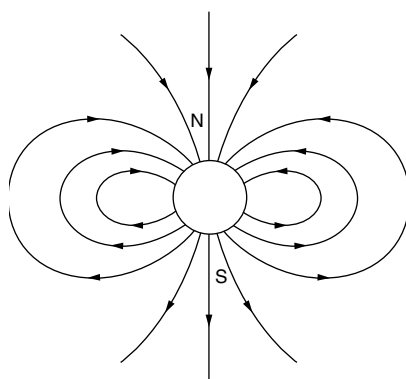
Figure 2.4.: Schematic illustration of a dipole magnetic field in vacuum (Figure from *Kelley* (2009)).

The field is created by currents in the molten, electrically conducting core of the Earth, which are in turn driven by thermal convection in the core. The convection is quite complex, but the dipole term is still the dominant term at the surface and the magnetic field contributions of higher order than the dipole term fall off faster with distance (*Kelley* (2009)).

But the Earth is not in vacuum, it is immersed in the atmosphere of the Sun and its magnetic field acts as an obstacle to the solar wind that cannot flow across the Earth's magnetic field lines. The bulk of the flow is deflected around the Earth leaving a magnetic cavity shaped like a comet head and tail, see Fig. 2.5 (*Schunk and Nagy* (2009)).

Figure 2.5.: Schematic illustration of the Earth's bow shock and magnetosphere (Figure from *Schunk and Nagy* (2009)).

On the sunward side of the Earth the solar wind pressure acts to compress the geomagnetic field and the head of the comet occurs, while the solar wind flowing past the Earth acts to produce an elongated tail on the side away from the Sun. A so called bow shock is formed when the supersonic solar wind hits the Earth's magnetic field. The location of this shock ma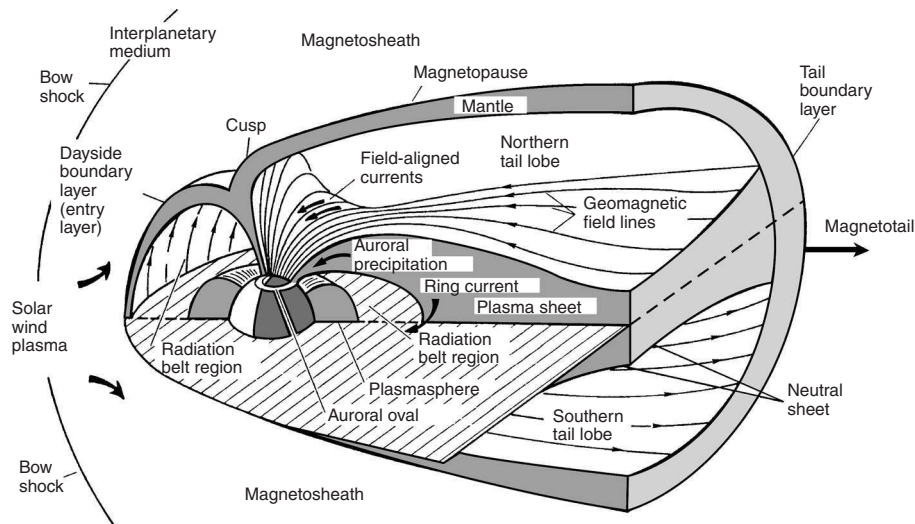y vary depending on the balance between the solar wind dynamic pressure and the magnetic pressure of the compressed geomagnetic field. Its shape and orientation also vary depending on both the direction of the IMF and the solar wind speed. The shock surface drapes around the Earth and it is symmetric with respect to the ecliptic plane. The average location of the closest point of the shock surface, the nose, is approximately 12 Earth radii from the Earth's surface.

As the solar wind passes through the bow shock, it is decelerated, heated, and deflected around the Earth in a region called the magnetosheath, its thickness is about 3 Earth radii near the subsolar point but it increases in the downstream direction. The heated solar wind plasma is then accelerated again to supersonic speeds as it moves past the Earth. The magnetized solar wind plasma in the magnetosheath is separated from that confined by the Earth's magnetic field by a boundary layer called the magnetopause. Its location is determined approximately by the balance between the dynamic pressure of the shocked solar wind and the magnetic pressure of the compressed geomagnetic field. On the sunward side of the Earth along the Earth–Sun direction, the magnetopause radial position is about 9 Earth radii (*Schunk and Nagy* (2009)).

Along the magnetopause an extensive current flows, it acts to separate the solar wind's magnetic field from the Earth's magnetic field. The magnetosphere is the region where the Earth's magnetic field dominates, it encircles the entire three-dimensional volume inside

the magnetopause and it is populated by thermal plasma and energetic charged particles of both solar and terrestrial origin.

On the day side, the polar cusp is where the solar wind plasma may enter the magnetosphere. Solar wind particles also get into the tail of the magnetosphere and they populate a region called the plasma sheet. The particles in the plasma sheet precipitate into the upper atmosphere of the Earth's along specific magnetic field lines on the night side. The particles precipitate in a ring around the polar regions which is narrow in latitude but extended in longitude around the Earth, the so called auroral oval (*Kelley* (2009)).

Across the plasma sheet the so called neutral current sheet flows from dawn to dusk near the magnetic equatorial plane. It acts to separate the two regions of oppositely directed magnetic fields in the magnetospheric tail; above the neutral current sheet, in the northern hemisphere, the magnetic field is toward the Earth and below the current sheet, in the southern hemisphere, it is away from the Earth. These magnetic field lines extend deep in the magnetospheric tail, but they get connected to the magnetic field embedded in the shocked solar wind and convect back to the Earth. This connection acts to generate potential drops in the magnetospheric tail that map down to the polar cap, the region poleward of the auroral oval. The electric field that is generated points from dawn to dusk across the polar cap (*Schunk and Nagy* (2009)).

The Van Allen radiation belts are the regions where the energetic particles that drift close to the Earth (due to magnetospheric electric fields) get trapped on closed geomagnetic field lines. They bounce back and forth between the northern and the southern hemispheres. Due to gradients in the geomagnetic field they also drift in an azimuthal direction around the Earth. The result of the drift of the lower energy particles is what is known as the ring current, a large-scale ring of current that encircles the Earth.

To respond to electric fields that penetrate at high-latitude, the electrons and protons in the ring current polarize and set up an oppositely directed electric field, which cancels the penetrating high-latitude electric fields. As a consequence the mid and low latitude regions are generally not affected by magnetospheric electric fields. Closer to the Earth is the plasmasphere, which is a toroidal region that surrounds the Earth and contains a relatively cool ($\sim 5000K$), high-density ($\sim 102cm^{-3}$) plasma which exchanges plasma with the Earth's ionosphere. The plasma in the plasmasphere co-rotates with the Earth, but it can also flow from one hemisphere to the other along geomagnetic field lines. The plasmapause is the boundary between the plasma that co-rotates with the Earth and the plasma that is influenced by magnetospheric electric fields. It is typically characterized by a large and sharp decrease in plasma density leaving the plasmasphere (*Schunk and Nagy* (2009)).

The main source of plasma close to the Earth is the Earth's atmosphere, we describe it in the next section.

2.2.2. The atmosphere, nomenclature and structure

"The atmosphere of the Earth is an ocean of gas encircling the globe. It stretches out into far distances from the surface; how far out is a question of definition" (*Brekke* (2012)).

In Fig. 2.6 it is shown a schematic illustration of the structure of the Earth's atmosphere. According to the variations in the composition we can identify two main regions in the Earth's atmosphere: the homosphere where the components are fully mixed in a homogeneous gas (below 100 km), and the heterosphere where the constituents behave independently and the gas is heterogeneous. At the ground the atmosphere is composed of close to 80% N_2 and 20% O_2, while the contribution from other gases is less than 1%. This mixture holds up to 100 km, in the homosphere. In the heterosphere different constituents are present and the composition differs depending on the solar activity: atomic oxygen dominates the upper atmosphere above 250 km during solar maximum conditions, hydrogen is more dominant above 400 km during minimum conditions. Independent on solar activity, below 200 km molecular oxygen and nitrogen together with argon are the dominant species (*Brekke* (2012)).
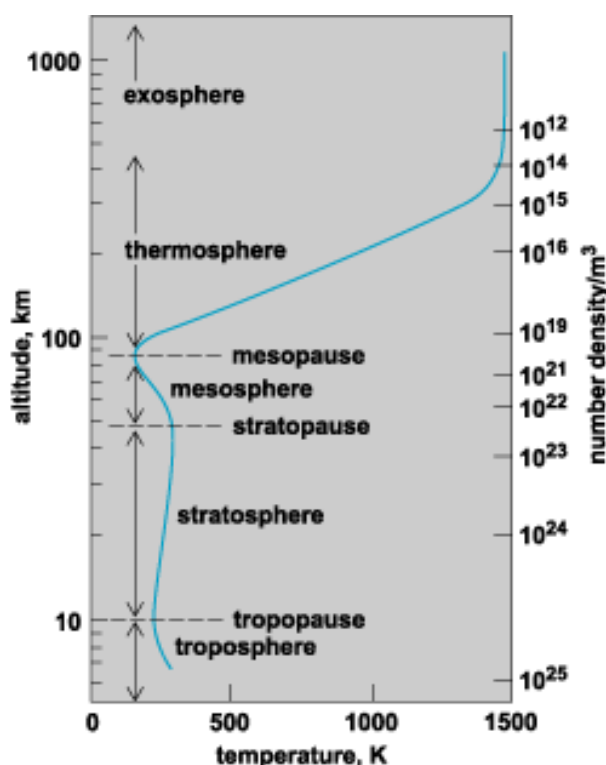
Figure 2.6.: Schematic illustration of the atmospheric temperature variation with altitude and constituent number density at high solar activity (Figure from http://www.answers.com/topic/aeronomy-1).

The number density of the atmosphere decreases monotonically by height from 10^{25} m^{-3} at ground level to 10^{14} m^{-3} at 400 km. The temperature behaves in a more complicated manner, it starts out by decreasing in the troposphere from about 290 K at ground level and it reaches a minimum close to 215 K at 15-20 km in the tropopause. In the stratosphere the temperature increases and it reaches a maximum close to 280 K around 50 km called the stratopause. In the mesosphere the temperature decreases again and it reaches the lowest temperature in the mesopause of about 160 K or even lower at occasions. In the termosphere then the temperature increases dramatically and temperatures higher than 1000 K can be found in the exosphere. Above this region the temperature is fairly constant

with height (*Brekke* (2012)).

2.2.3. The ionosphere

The ionosphere is the ionized portion of the upper atmosphere of the Earth. It completely encircles the Earth and it extends from about 60 km up to 1000 km. The photoionization of neutral molecules is the main source of plasma in the ionosphere. Then several processes may occur: chemical reactions between the ions produced and the neutrals take place, ions recombine with the electrons, ions diffuse to either higher or lower altitudes, or they are transported via neutral wind effects. Notice that the Earth's intrinsic magnetic field, which is dipolar at ionospheric altitudes, strongly influences the diffusion and transport effects (*Schunk and Nagy* (2009)).

At different latitudes, different physical processes dominate, but the electron density variation with altitude still displays the same basic structure except that at high latitudes at high altitudes the O^+ density differs from that at mid-latitudes. This structure is layered in distinct regions: D, E, F_1 and F_2, in Fig. 2.7 it is shown the electron density profile at mid-latitudes.
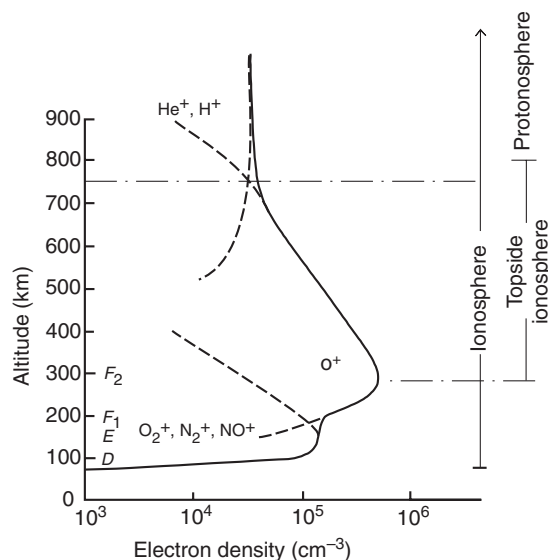
Figure 2.7.: Ion density profiles for the daytime mid-latitude ionosphere showing the different layers (Figure from *Schunk and Nagy* (2009)).

In the D and E regions molecular ions dominate, N_2, O_2 and O are the most abundant neutral species and chemical processes are the most important. In the D region there are both positive and negative ions, water cluster ions and three-body chemical reactions. The D region presents a complicated chemistry, therefor, sometimes the lower D-region may be referred to as C region. In the E region the chemical reactions are not that complicated, the plasma is weakly ionized and collisions between charged particles are not important. In the F_1 region ion-neutral interchange and transport processes start to be important, and in the F_2 region the ionization maximum occurs because the plasma transport is balanced

by the chemical loss processes. In these regions O^+ and O atomic species dominate. Something important to note is that the peak in the ion density in the F_2 region is roughly a factor of 10 greater than that in the E region, while the neutral density is 2 orders of magnitude greater than the ion density. In this region the plasma is partially ionized and collisions between charged particles and between charged particles and neutrals cannot be neglected.

The region above the F-peak is called the topside ionosphere, while the region where lighter atomic ions H^+ and He^+ dominate is called the protonsphere. The plasma is fully ionized, only collisions between charged particles must be taken into account and plasma transport processes dominate (*Schunk and Nagy* (2009)).

The temperature of the ionosphere is mainly controlled by the absorption of solar UV (UltraViolet) radiation in the thermosphere. The temperature of the electrons is usually higher than the ion temperature because the electrons have a larger mobility and heat conductivity. The ion temperature is higher than the neutral temperature because the ions are heavier and interact by collisions more strongly with the neutral gas and much of the excess energy of the ions is transferred to the neutral gas (*Brekke* (2012)).

In the topside ionosphere, the ion distribution is controlled by mechanical forces: electric and magnetic fields, gravity, ion pressure gradient and centrifugal force. The behavior of the F_2 region and the topside ionosphere are strongly coupled, this coupling is due to the fact that the ionosphere at lower altitudes is a source and sink for the topside plasma. From the topside ionosphere permanent loss of ionospheric plasma may occur because of electric fields of magnetospheric origin (*Banks and Kockarts* (1973)).

In the topside ionosphere plasma can be in three diffusive states (*Banks and Kockarts* (1973)):

1. Diffusive equilibrium, which corresponds to no net transport of ionization along a magnetic field tube (this state is seldom reached).

2. Inward diffusive flow, which corresponds to an excess of plasma pressure at high altitudes at some point along a magnetic field tube resulting in net downward transport of the light ions from the topside. The result is in general an enhancement in the F_2 region ion density.

3. Outward diffusive flow, which corresponds to a deficit of plasma pressure at some point along a magnetic field tube resulting in net outward transport of the light ions.

The dynamical properties of the topside ionosphere are complex and while at low latitudes there are opportunities to reach the diffusive equilibrium state, at mid and high latitudes it appears that plasma outflow or inflow take place (*Banks and Kockarts* (1973)).

2.3. Ion outflows

2.3.1. Overview

Observational and theoretical research have already established that the ionosphere is a significant source of plasma for the magnetosphere. At high altitudes (>2000 km) the

classical polar wind, which is the flow of ionospheric thermal plasma into the magneto-sphere on open geomagnetic field lines, supplies the magnetosphere with mainly H^+, He^+ and O^+ ions with bulk speeds that may reach the gravitational escape speed. In addition, plasma waves and parallel electric fields accelerate ions giving rise to suprathermal out-flowing ions in the form of conics and field-aligned beams respectively (*Burchill et al.* (2010) and references therein).

The high-altitude outflows are in part regulated by the supply of thermal plasma from below, via the motion of the F region and topside ionospheric plasma along the magnetic field lines at mid and high latitudes (*Burchill et al.* (2010) and references therein).

Ground-based radars and orbiting spacecraft have observed low-altitude outflows (<2000 km) at mid and high latitudes reaching speeds of up to 1 kms^{-1}or even greater at times (*Burchill et al.* (2010) and references therein).

In this thesis we only study low-altitudes ion outflows.

2.3.2. Basic equations

In the topside ionosphere the ion density profile can be determined from the continuity and momentum equations for each ion species (*Banks and Kockarts* (1973)).

For the j-th species the one-dimensional continuity equation parallel to the magnetic field lines is:

$$\frac{\partial n_j^+}{\partial t} + \frac{1}{A}\frac{\partial\left(n_j^+ w_j A\right)}{\partial s} = q_j - l_j \tag{2.1}$$

where n_j^+ is the j-th ion species density, w_j is the ion bulk transport velocity parallel to the magnetic field direction of the j-th ion species, s is a coordinate along the magnetic field, A is the area of the magnetic field flux tube at the point s, q_j is the production rate of the j-th ion species and l_j is the loss rate of the j-th ion species.

For the j-th species the one-dimensional momentum equation parallel to the magnetic field lines is:

$$\frac{\partial w_j}{\partial t} + w_j\frac{\partial w_j}{\partial s} + \frac{1}{n_j^+ m_j}\frac{\partial p_j}{\partial s} + g_\parallel - \frac{Z_j e E_\parallel}{m_j} = -\sum_k \nu_{jk}\left(w_j - w_k\right) \tag{2.2}$$

where $p_j = n_j^+ k T_j$, $Z_j e$ is the ion atomic charge, $g_\parallel$ is the acceleration of gravity parallel to the magnetic field (here it is positive inwards), w_j, n_j^+ and s are defined as above, w_k is the parallel component of the velocity of the other ion and neutral species, ν_{jk} is the ion collision frequency between the j-th and the k-th species. The collision term includes the effects of ion-ion and ion-neutral collisions which retard or enhance the j-th ion bulk velocity. We have not included the effects of the centrifugal force.

The electron momentum equation to a high degree of approximation is:

$$\frac{1}{n_e}\frac{\partial p_e}{\partial s} + eE_\parallel = 0 \tag{2.3}$$

this means that in the topside ionosphere the parallel electric field induced by charge separation and the pressure gradient dominate and the gravity, the inertial and frictional effects are unimportant for the electron gas (*Banks and Kockarts* (1973)).

Substituting (2.3) into (2.2) the momentum equation for a multiconstituent plasma is:

$$\frac{\partial w_j}{\partial t} + w_j\frac{\partial w_j}{\partial s} + \frac{1}{n_j^+ m_j}\frac{\partial p_j}{\partial s} + g_\parallel + \frac{Z_j e E_\parallel}{n_e m_j}\frac{\partial p_e}{\partial s} = -\sum_k \nu_{jk}\left(w_j - w_k\right) \tag{2.4}$$

with the restraint of local charge neutrality:

$$n_e = \sum_k Z_j n_j^+ \tag{2.5}$$

The analytical solution for (2.1) and (2.4) is difficult to achieve, therefor either approximations or numerical models are needed in order to solve the equations to obtain the flow velocities and densities.

2.3.3. Wahlund's characterization

Two different types of low-altitude ion outflows have been identified: the first type (in the following they will be referred to as type-I ion outflow) is related to strong perpendicular electric fields, enhanced and anisotropic ion temperature and low electron density below 300 km, indicating small amounts of particle precipitation; the second type (in the following they will be referred to as type-II ion outflow) is related to auroral arcs and enhanced electron temperatures (*Wahlund et al.* (1992b)).

During the event of type-I ion outflow, they measured an increase in the ion temperature which occurred simultaneously with a decrease in the E region electron density indicating little auroral precipitation. At the same time, they observed a "lifting" upward of the F region and the electron temperature was hardly affected at all.

They observed that the enhancement in the ion temperature occurred at the same time the electric field raised. They also observed that the perpendicular ion temperature was higher than the parallel ion temperature (here perpendicular or parallel are with respect to the geomagnetic field) of about 300 K. They also argue that this anisotropic ion temperature enhancement indicates strong frictional heating under the influence of large electric fields.

Wahlund et al. (1992b) observed then two clear events of type-II ion outflows that were both related to a strong enhancement in the electron temperature, moderate perpendicular

electric field strengths and signatures of auroral precipitation. Moreover, only a slight increase in the ion temperature was observed before the outflows started.

During periods of type-II ion outflows, *Wahlund et al.* (1992b) also observed NEIALs, which are powerful echoes with Doppler shifts centered on the ion acoustic speed of the medium that exhibit a dramatic enhancement in power over a narrow range of frequencies when compared with "normal" spectra (see *Sedgemore-Schulthess and St. Maurice* (2001) and references therein). For more information about NEIALs see section sec. 2.4.

In Fig. 2.8 it is shown an example of type-I ion outflow detected with the ESR radar in our work. The event occurs in the evening sector, the ion drift velocity is plotted in the fourth panel.
In the first panel of the colour plot it is shown the electron density, which is low below 200-250 km. In the second panel the electron temperature is plotted. In this case it is fairly low, but at times it may be enhanced albeit remaining lower than the ion temperature. In the third panel the ion temperature is shown, note that it is clearly enhanced.

In Fig. 2.9 it is shown an example of type-II ion outflow detected with the ESR radar. The event occurs in the morning sector between 1100 UT and 1200 UT, the ion drift velocity is plotted in the fourth panel.
In the first panel of the colour plot it is shown the electron density. In contrast with type-I ion outflows, in type-II ion outflows the electron density is typically enhanced below 200-250 km. In the second panel the electron temperature is plotted, note that it is clearly enhanced. In the third panel the ion temperature is shown, and it is not enhanced.

2.3.4. Acceleration mechanisms

Since the aim of this thesis is to investigate type-I ion outflows, we only describe the acceleration mechanisms believed to be the sources of type-I ion outflows. See *Wahlund et al.* (1992b) and references therein for a treatment of the acceleration mechanisms of type-II ion outflows.

Jones et al. (1988) observed upwards acceleration of ions with velocities as high as 500 ms^{-1}. They suggest four factors to determine the observed field-aligned velocity:

1. the meridional component of the neutral wind;

2. the vertical upwelling of the neutral atmosphere as the consequence of strong and localized Joule heating;

3. the gradient of plasma pressure in the topside ionosphere;

4. the gravity.

During quiet conditions 1), 2) and 4) combine to drive a low flux of light ions from the top of the ionosphere, but large electric fields can cause strong Joule heating of the neutral atmosphere in the upper E region during disturbed conditions. *Jones et al.* (1988) argue that typical conditions lead to upward velocities of 50-100 ms^{-1}, they also state that although such an initial velocity is essential to greater accelerations, these factors cannot explain upward velocities of 500 ms^{-1}.
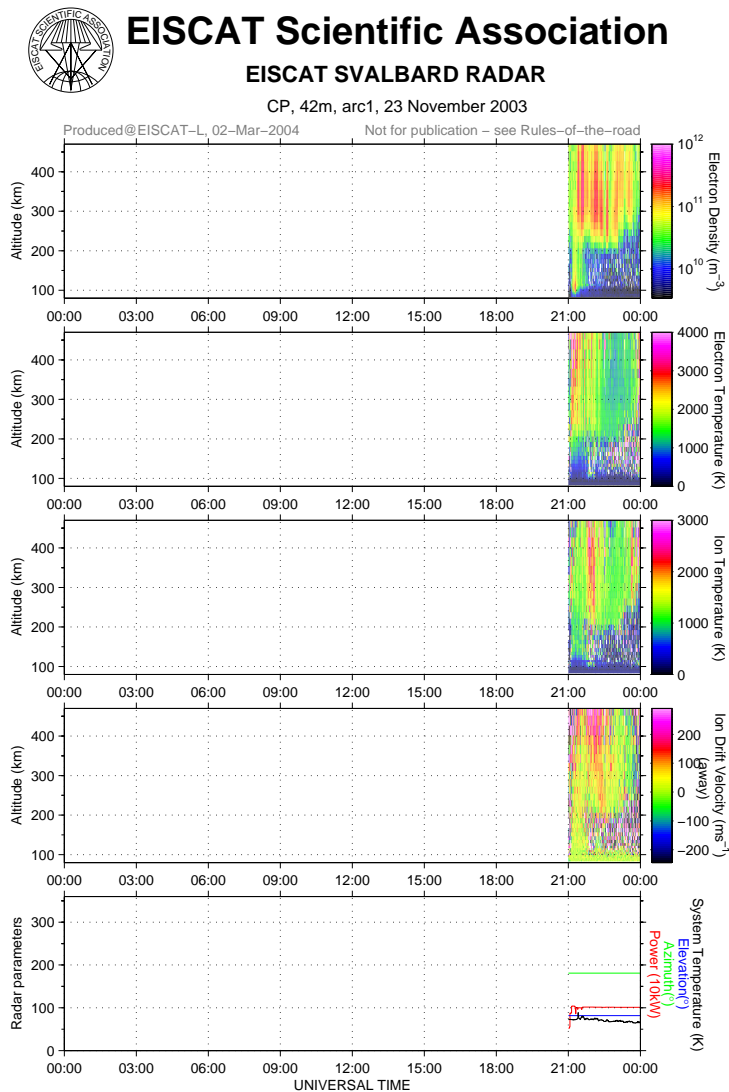
Figure 2.8.: Typical type-I ion outflow detected with the ESR radar on 23-11-2003 (colour plot from the EISCAT Madrigal database).

When the magnetospheric electric field is strong enough to drive the plasma in a direction perpendicular to the magnetic field line at a speed greater than the ion-acoustic speed, the ion velocity distribution changes from being a maxwellian distribution to a toroidal one (*Jones et al.* (1988) and references therein). When the distribution is anisotropic, a hydrodynamic mirror force acts on the plasma in addition to the enhancement in the pressure gradient from the increase in the parallel ion temperature (*Jones et al.* (1988)).

Jones et al. (1988) determined the gradient of pressure and the mirror force, and their predicted height profile of the upward plasma velocity agreed with the observations.

In the literature, particle precipitation have often been proposed to be an important acceleration mechanism that leads to ion outflows. Soft electron (<1 keV) precipitation and or heat conduction are believed to increase the temperature of the ionospheric electrons, leading to an enhancement of the ambipolar electric field which then accelerates ions upward (*Burchill et al.* (2010) and references therein).
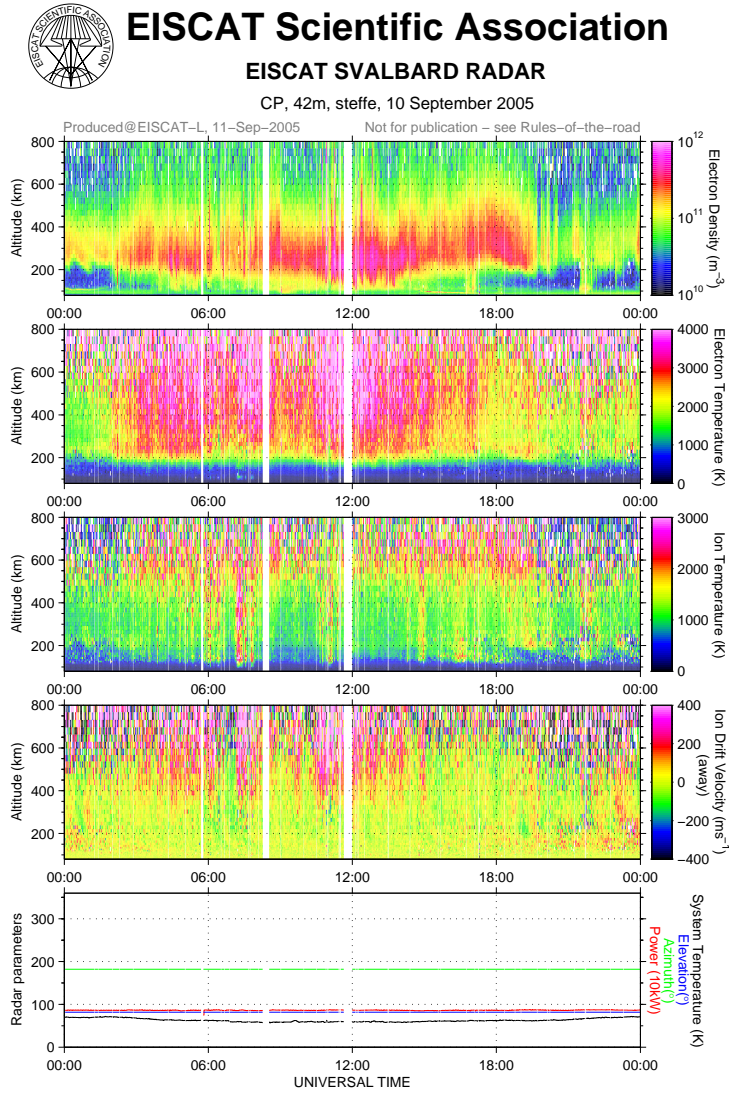
Figure 2.9.: Typical type-II ion outflow detected with the ESR radar on 10-09-2005 (colour plot from the EISCAT Madrigal database).

2.3.5. Ion heating

At high latitudes, the main mechanisms responsible for the ion heating are frictional heating and heat exchange with the neutral gas and the electron gas. When a relative velocity between the ions and the neutral gas exists, frictional heating occurs. It is well described as Joule heating due to Pedersen currents $J_P = \sigma_P E$ (*Kelley* (2009)). When all these effects are considered, the ion temperature can be described as:

$$T_i = T_{eq} + \frac{m_n \phi_{in}}{3k\varphi_{in}} |V_i - V_n|^2 \tag{2.6}$$

where m_n is the neutral mass, k is the Boltzmann's constant, V_i and V_n are the ion and

neutral velocities respectively and

$$T_{eq} = T_n + \left[(m_i + m_n) \frac{v_{ie}}{m_i v_{in} \varphi_{in}} \right] (T_e - T_i) \qquad (2.7)$$

The dimensionless ϕ_{in} and φ_{in} depend on the nature of the collisional interactions between the ions and the neutral gas, above about 200 km they are approximately unity (*Kelley* (2009)). These expressions show that when $|V_i - V_n| \neq 0$ (i.e. when a relative velocity between the ions and the neutral gas exists) the ion temperature will increase from its equilibrium value.

However, at high latitudes it may occur that the neutral gas is set in motion by the same ion-neutral collisions that produce frictional heating of the ion gas, resulting in an equalization of the ion and neutral velocities in a steady state. If this occurs, the ion gas can be moving quite rapidly with almost no frictional heating (*Kelley* (2009)).

Furthermore, *Amatucci et al.* (1998) argue that sounding rocket experiments and satellite data provide compelling evidence of a correlation between small-scale spatial inhomogeneities, broadband low-frequency waves and transversely heated ions. Referring to the model made by *Ganguli et al.* (1994), they state that the non-linear steepening of a low-frequency wave can lead to strongly localized electric fields which are likely to be randomly distributed in space, and because of this, ions may receive varying amounts of energy from each individual layer by successive interactions (*Amatucci et al.* (1998)). In their experiment, *Amatucci et al.* (1998) isolated one such layer to investigate the physics of ion energization. Their results show that even when a large electric field is present, the ion temperature remains equal to its equilibrium value prior the wave onset and ion heating occurs once waves are present.

Also *Wahlund et al.* (1998) reported that broadband extremely low-frequency (hereafter refer to as BB-ELF) emissions are associated with intense events of transverse ion acceleration. BB-ELF covers frequencies from 0 to few kHz and have been found to consist of different wave modes occurring at the same time. Moreover, they are thought to be of different origin (*Wahlund et al.* (1998)). *Wahlund et al.* (1998) presented satellite measurements of BB-ELF plasma waves together with intense transverse O^+ energization. They showed that the range 30-400 Hz is dominated by slow ion-acoustic waves and they argue that the often simultaneous presence of Alfvénic wave activity or large-amplitude electric fields suggest that these phenomena provides the original free energy for the BB-ELF emission which in turn transversely heat the O^+ ions (*Wahlund et al.* (1998)).

2.4. NEIALs

2.4.1. General

Incoherent scatter spectra are usually associated with near-maxwellian plasmas where the electron temperature is higher than the ion temperature and they typically display a two-shouldered form (see sec. 3.1.2) (*Hagfors* (1995)). Clear departures from these

"normal" spectra are often observed along the geomagnetic field lines, showing an evident enhancement in one or both of the ion acoustic shoulders in the power spectrum, see Fig. 2.10. These events are usually short-lived, at most they last for a few tens of seconds (*Grydeland et al.* (2003) and *Michell et al.* (2009)). Such enhancements may also be associated to hard-targets, for example Earth-orbiting satellites (*Rietveld et al.* (1991)), but in this thesis we only focus on "naturally" enhanced spectra.
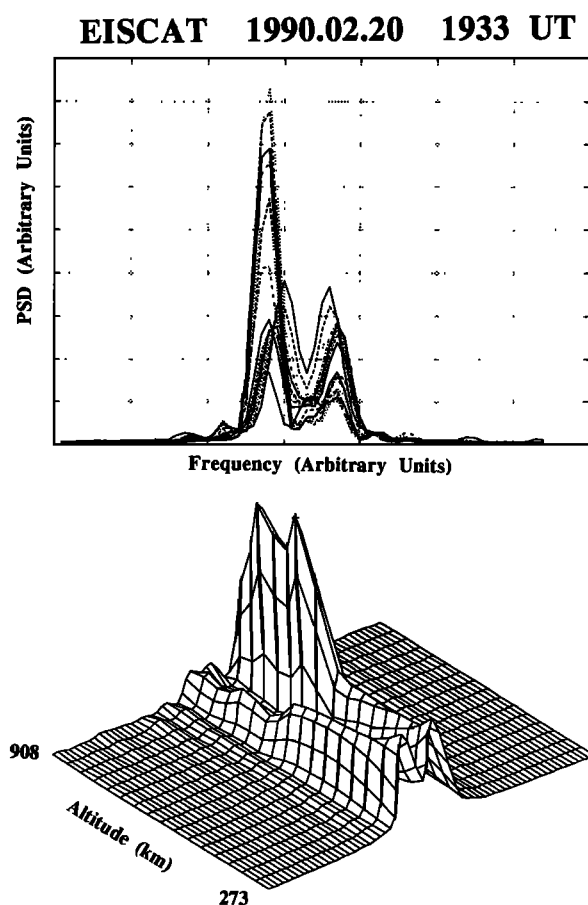

Figure 2.10.: NEIAL observed during a type-II ion outflow event reported by *Wahlund et al.* (1992b) (Figure from *Wahlund et al.* (1992b)).

According to *Sedgemore-Schulthess and St. Maurice* (2001) NEIALs are related with several phenomena: high electron temperature, strong ion upflows above 300 km and echo location on the edge of discrete precipitation structures. Moreover others features may be added: NEIALs are thought to occur more frequently at higher altitudes, down-shifted ion acoustic waves often tend to be enhanced over the up-shifted ones at higher altitudes, and NEIALs are observed at longer radar wavelengths with a greater probability (*Sedgemore-Schulthess and St. Maurice* (2001)).

The generation mechanism of NEIALs is still not fully understood, many theories have been proposed in the last years. At the present time three of them appear to be more accredited: the current-driven instability theory based on intense current densities along the magnetic field (*Rietveld et al.* (1991)), the parametric decay of Langmuir waves theory

(*Forme* (1993)) and the third one is the ion-ion two-stream instability theory (*Wahlund et al.* (1992a)).

2.4.2. The current driven instability theory

Rietveld et al. (1991) report observations made with the UHF radar (see sec. 3.1.1 for information about the UHF radar) of NEIALs over altitudes going from 138 km to 586 km along the magnetic field direction. They argue that even though there are similarities, these echoes are clearly inconsistent with satellite echoes. This is because the observed NEIALs come from a very extended height range while satellite echoes are usually limited in the range extent (*Rietveld et al.* (1991)). Satellite echoes also show a more square-like signature in the power profile.

The observed enhancements in the ion-acoustic shoulders are related with geomagnetic disturbances, high electron temperatures and a temperature ratio T_e/T_i typically of 2-3 before the echoes, auroral arcs and red aurora in the F region and field-aligned ion outflows appearing to be a type-II ion outflow (see sec. 2.3.3).

Rietveld et al. (1991) argue that the observed echoes can simply be due to a strong field-aligned motion in the thermal electrons. The consequence is that in the F region of the ionosphere, there must be strong electric fields to sustain such currents. *Rietveld et al.* (1991) identified beam electrons carrying parallel currents as the likely generator. The consequence is that in the F region, strong parallel electric fields are possible and should be triggered with sufficient intensity in the presence of intense soft electron fluxes.
Rietveld et al. (1991) claim that simulations show that large thermal electron fluxes of more than 1 mAm^{-2} are the cause of the enhanced ion acoustic shoulders and they suggest that field-aligned flows of soft electrons which deposit energy to the horizontally poor conducting F region heights are the cause of parallel electric fields in the ionosphere. These fields produce thermal electron motions that they argue are the cause of the observed NEIALs (*Rietveld et al.* (1991)).

2.4.3. The parametric decay of Langmuir waves theory

Forme (1993) give another interpretation on the origin of NEIALs. They state that the two interpretations presented by *Rietveld et al.* (1991) and *Wahlund et al.* (1992a) (see sec. 2.4.2 and sec. 2.4.4, respectively) have problems in explaining the whole observations like ion-acoustic waves propagating simultaneously in parallel and antiparallel directions.

They suggest that ion acoustic waves are the result of the parametric decay of beam generated Langmuir waves. They argue that Langmuir waves may be excited by a beam instability due to electron beams at energies of 10 to 500 eV and that this instability may occur in the upper ionosphere for reasonable electron beam and ionospheric parameters (*Forme* (1993)). Their model predicts electric field amplitudes of 1 to 100 mV/m for ion acoustic and Langmuir waves, respectively.

Moreover, *Forme* (1993) state that downward going ion acoustic waves are due to precipitating electrons, while upward going acoustic waves are thought to be present when large fluxes of backscattered electrons and secondary electrons are present.

Forme (1993) also claim that the estimations of electron energy and flux as well as the wave amplitude are in good agreement with the observations found in the literature.

2.4.4. The ion-ion two-stream instability theory

Wahlund et al. (1992a) claim that NEIALs can be produced in a plasma unstable to the ion-ion two-stream instability. This instability occurs when a relative drift between two ion populations exists. They argue that taking into account several ion species abundances, temperature ratios T_e/T_i and ion drifts, many of the observed NEIALs with the EISCAT and Millstone Hill radars (*Foster et al.* (1988)) can be explained by the two-stream instability theory.

Wahlund et al. (1992a) state that the mechanism they propose is in good agreement with both the observations of spectral features and with observed occurrence conditions of the typical parameters within auroras in the topside ionosphere. They also state that the good correlation of ion outflows with low energy particle precipitation and NEIALs support the ion-ion two-stream instability theory.

3. Instrumentation and method

In this chapter an overview of the instrumentation used together with an explanation of the incoherent scatter radar technique are given in the first section. A description of the method used to identify type-I ion outflows follows in the second section.

3.1. The EISCAT system

3.1.1. General about EISCAT

EISCAT is the European Incoherent SCATter Scientific Association established to conduct research in the lower, middle and upper atmosphere and ionosphere using the incoherent scatter radar technique (see sec. 3.1.2) (http://www.eiscat.se/).

There are ten incoherent scatter radars in the world, and EISCAT operates three of the highest-standard facilities. The experimental sites of EISCAT are located in the Scandinavian sector, north of the Arctic Circle.

The EISCAT UHF (Ultra High Frequency) radar operates in the 931 MHz band with a peak transmitter power of more than 2.0 MW and 32 m, fully steerable parabolic dish antennas. The transmitter and one receiver are in Tromsø (Norway). Receiving sites are also located near Kiruna (Sweden) and Sodankylä (Finland), allowing continuous tristatic measurements to be made (http://www.eiscat.se/).

The monostatic VHF (Very High Frequency) radar in Tromsø operates in the 224 MHz band with a peak transmitter power of 2 x 1.5 MW and a 120 m x 40 m parabolic cylinder antenna, which is subdivided into four sectors. It can be steered mechanically in the meridional plane from vertical to 60° north of the zenith; limited east-west steering is also possible using alternative phasing cable (http://www.eiscat.se/).

The ESR (EISCAT Svalbard Radar), located near Longyearbyen, operates in the 500 MHz band with a peak transmitter power of 1.0 MW, a fully steerable parabolic dish antenna of 32 m diameter, and a fixed field aligned antenna of 42 m diameter. The high latitude location of this facility is particularly aimed at studies of the cusp and polar cap region (http://www.eiscat.se/).

In Tab. 3.1 are listed the coordinates of the EISCAT facilities, in this thesis we use data obtained from the UHF, the VHF and the ESR radars.

In Tab. 3.2 the main technical specifications of the UHF, the VHF and the ESR radars are listed. For more information about the EISCAT facilities visit the website (http://www.eiscat.se/).

Location	Tromsø	Longyearbyen
Geographic latitude	69° 35' N (69.58°)	78° 09' N (78.15°)
Geographic longitude	19° 14' E (19.23°)	16° 01' E (16.02°)
Altitude	86 m	445 m
Corrected geomagnetic latitude	66.73°	75.43°
Corrected geomagnetic longitude	102.18°	110.68°

Table 3.1.: Location of the EISCAT facilities (http://www.eiscat.se/).

	UHF	VHF	ESR
Transmitter frequencies	926.6 - 930.5 MHz	222.8 - 225.4 MHz	498.0 - 502.0 MHz
Peak power	2 MW	1.6 MW	1 MW
Receiver frequencies	921.0-933.5 MHz	214.3 - 234.7 MHz	485.0 - 515.0 MHz
Antenna	32 m steerable parabolic dish	Four 30×40 m steerable parabolic cylinders	42 m fixed and 32 m steerable parabolic dishes

Table 3.2.: Technical specifications of the UHF, the VHF and the ESR radars (http://www.eiscat.se/).

3.1.2. The incoherent scatter radar technique

In 1906 J. J. Thomson showed that free electrons are capable of scattering electromagnetic radiation in a particular direction with a scattering cross section given by (*Beynon and Williams* (1978)):

$$\sigma = 4\pi(r_e \sin\gamma)^2 \tag{3.1}$$

where r_e is the radius of the electron and γ is the angle between the direction of the incident electric field and the direction to the observer. For a direct back-scatter, we have $\gamma = 90$ and a free electron has a scattering cross section of $\sigma_e = 0.998 \times 10^{-28} m^2$ (*Beynon and Williams* (1978)).

C. Fabry (*Fabry* (1928)) suggested that the scattering of electromagnetic waves by free electrons in the ionosphere might be significant at radio frequencies and he pointed out that the scattered signal from electrons possibly illuminated by a monochromatic beam would show a Doppler broadening corresponding to their thermal velocity. Fabry only underlined that the scattering cross section of electrons was extremely small and he made no attempt to estimate the strength of the scattered radio signal for a transmitter of given power: anyway, it would have not been possible to detect such weak signals with the transmitter power and receiver sensitivities available at that time.

W. E. Gordon in 1958 suggested that it would have been possible to detect the Thomson scattering of radar signals from the ionosphere and to measure both the electron density and the electron temperature as a function of altitude using a "large enough antenna" (*Gordon* (1958)).

Due to electrostatic interactions between electrons and positively charged ions in the ionosphere it is incorrect to consider free electrons. Because of these electrostatic forces, ions tend to be attracted by each electron and at the same time their thermal velocity and their mutual repulsion tend to disperse them. The result is that the ions form a shield around each electron and the scale of this shield depends on the balance between random thermal energy and electrostatic potential energy (*Beynon and Williams* (1978)). The scale of this shield is represented by the Debye length:

$$\lambda_D = \left(\frac{\varepsilon_0 k T_e}{n_e^2} \right)^{1/2} \tag{3.2}$$

where T_e and n_e are the electron temperature and the electron density, respectively.

Usually, the radar wavelength is much greater than λ_D and we can no longer consider scattering from free and independent electrons because the surrounding ions strongly control the movements of the electrons. The result of this electrostatic coupling is that the random thermal motions of the electrons generate waves in the plasma known as "ion-acoustic" waves and "electron-acoustic" or "plasma" waves. "Acoustic" because these waves resemble acoustic waves in a neutral gas where pressure gradients give rise to longitudinal waves. Such waves occur in a plasma, but to properly treat them we need to add the electrostatic forces to the forces due to pressure gradients because when the density of ions (or electrons) increases locally a net electric charge is produced. It is the fluctuation of the electron density caused by such waves that gives rise to the observed scattered signals (*Beynon and Williams* (1978)).

The typical incoherent scatter spectrum consists of a double-humped ion spectrum, distributed on either side of the transmitted frequency f, and two sharp plasma lines at frequencies $f \pm F^-(\Lambda)$ where $F^-(\Lambda)$ is the frequency of the electron-acoustic waves, see Fig. 3.1 (see *Beynon and Williams* (1978) for more details on the incoherent spectrum).

Most of the research with incoherent scatter radars concerns the ion spectrum because the plasma lines are more difficult to observe.

The area of the ion spectrum represents the total power received and from it, the electron density can be derived. The line of sight velocity of the ion-acoustic wave is given by the frequency shift of the spectrum, this velocity corresponds to bulk ion motion in the direction of the radar beam (*Sedgemore-Schulthess and St. Maurice* (2001)). The sharpness of the ion line peaks gives the temperature ratio T_e/T_i and their separation is proportional to $(T_i/m_i)^{1/2}$ (*Sedgemore-Schulthess and St. Maurice* (2001)).

The shape of the ion spectrum depends on several ionospheric parameters. The effect of the various plasma parameters on the shape of the spectrum are shown in Fig. 3.2. The first panel shows the effect of ion temperature with a constant temperature ratio T_e/T_i of unity and zero ion-neutral collision frequency: increasing the ion temperature, the "shoulders"
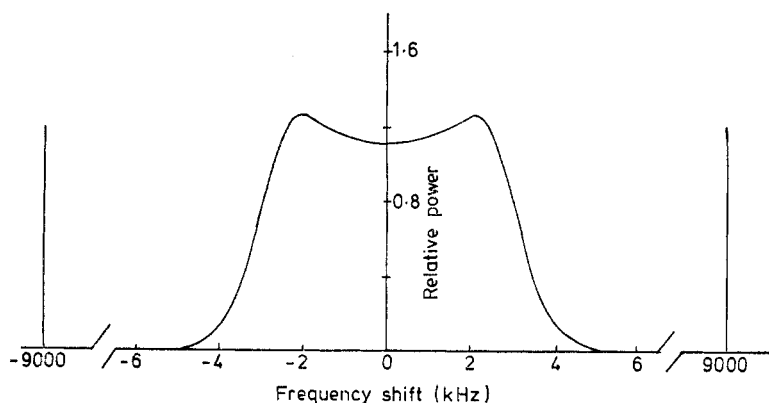
Figure 3.1.: Ion spectrum and plasma line for $n = 10^{12} m^{-3}$, $T_e = 1000K$ and $T_i = 1000K$. (Figure from *Beynon and Williams* (1978)).

of the spectrum move outward from the radar frequency and the ion line broadens. In the second panel the ion temperature is kept constant and the temperature ratio varies: increasing the temperature ratio leads to a deeper "valley". The third panel shows the effect of ion collisions keeping the temperatures fixed: increasing the collision frequency the minimum at the center of the spectrum becomes more shallow until it completely disappears. In the last panel we can see the effect of the ion mass on the spectrum: decreasing the ion mass leads to a widening of the spectrum (*Nygrén* (1996)).

3.2. Identification of type-I ion outflows

We used data from the Madrigal database which is an upper atmospheric science database used by groups throughout the world. Madrigal is World Wide Web based system capable of managing and serving archival and real-time data, in several formats, from a wide range of upper atmospheric science instruments (http://cedar.openmadrigal.org/). In particular we used the EISCAT data starting from January 2000 to December 2010, considering only field-aligned experiments ran from the UHF, the VHF and the ESR radars.

As we described in sec. 2.3.3, type-I outflows are characterized by strong perpendicular electric fields, enhanced and anisotropic ion temperatures and low electron densities below 300 km. To identify type-I outflows we needed the colour plots of the electron density, the ion velocity and both the electron and ion temperatures. Therefore, we only used experiments where the colour plots were already available. Starting from these plots, it was possible to identify the outflow events and see whether the electron density was low or not and if the enhancement in the ion temperature was present. But without using experiments from the tristatic system it was not possible to measure the ion temperature perpendicular to the geomagnetic field. We did not use experiments from the tristatic radar because it was beyond the time limit of this thesis. So hereafter we consider as type-I outflows only the events where the ion temperature is higher than the electron temperature along the magnetic field and, we do not say anything about the potential anisotropy of the ion temperature.
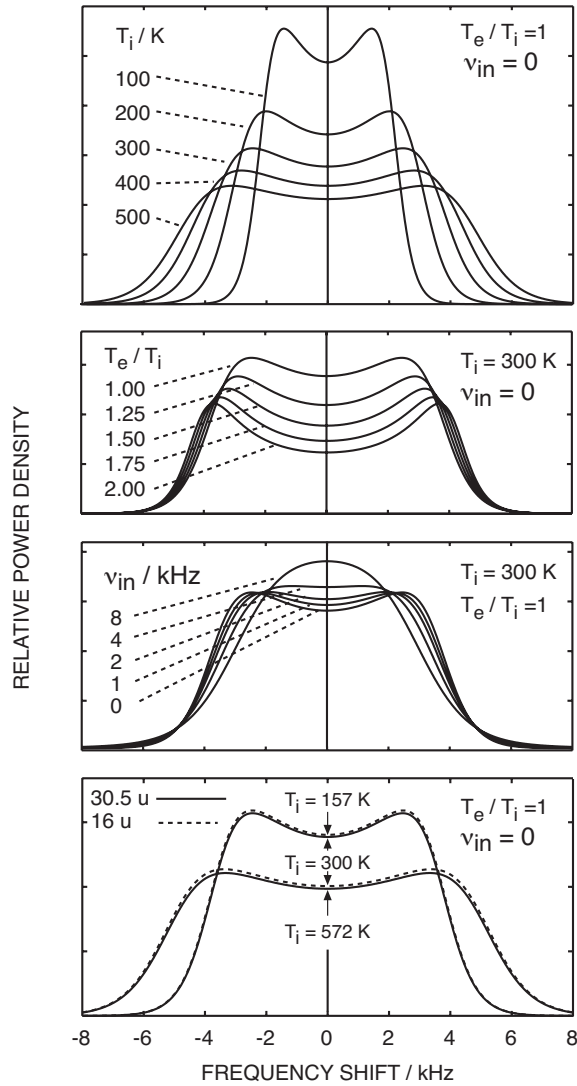
Figure 3.2.: Ion spectrum depending on plasma parameters (Figure from *Nygrén* (1996)).

When all the potential type-I outflow candidates were identified, we analyzed the data using a matlab program that plotted the temperature ratio (T_e/T_i).

We counted how many days per year each radar was on and we separated them in three categories:

1. days when at least one outflow event was present;

2. days when at least one type-I outflow was detected;

3. days when either no outflow events were detected or with noisy data (here noisy means that the signal to noise ratio is low and the colour plot is too scattered).

Notice that we did not count the number of outflows, this means that during one day there could be more than one outflow. Moreover, several days when a type-I outflow was detected were also characterized by the presence of other types of outflow.

We chose to merge the noisy days and the days when no outflows were present because

very often a single day was noisy at a certain time and no outflow was present at a different time.

4. Observations

In this chapter we first describe the type-I outflows we identified with the UHF, the VHF and the ESR radars, trying to give the occurrence frequency of them during the period considered (January 2000 - December 2010). In the second section we describe the results obtained in the attempt to find NEIALs during the type-I outflows. In the last section we describe a third type of outflow identified.

4.1. Type-I outflows identified

Once we analyzed data from the dates where type-I outflows were detected we identify two different types of situations:

- outflows characterized by a temperature ratio $T_e/T_i < 1$ all the time and at all altitudes. We will refer to such events as continuous type-I outflows;

- outflow events when the temperature ratio changes either in time or in altitude and outflow events when the temperature ratio changes both in time and altitude. We will refer to these outflows as non-continuous type-I outflows.

In the following, we describe separately the results obtained with the three incoherent radars.

Notice that all the colour plots that follow have been obtained using a matlab program (see Appendix A) and all of them show block numbers in the time axis, the actual time intervals when the events detected by the UHF, VHF and ESR radars are listed in Tab. 4.1, Tab. 4.2 and Tab. 4.3, respectively.

4.1.1. UHF radar

As we mentioned in sec. 3.2 we considered only experiments where the colour plots were already available and were the radar was field-aligned which means that the beam is aligned with the geomagnetic field lines. In the case of the UHF radar we only used experiments where the elevation angle was fixed at: ~ 77, ~ 81 or ~ 90 degrees.

The results are summarized in the histogram in Fig. 4.1. The blue columns show the number of days where the UHF radar was on. In this number only days where field-aligned experiments were ran are included. The red columns show the number of days where outflows have been detected. This number includes type-II ion outflows and flickering outflows (see sec. 4.3). The yellow columns show the number of days where type-I ion outflows have been identified.
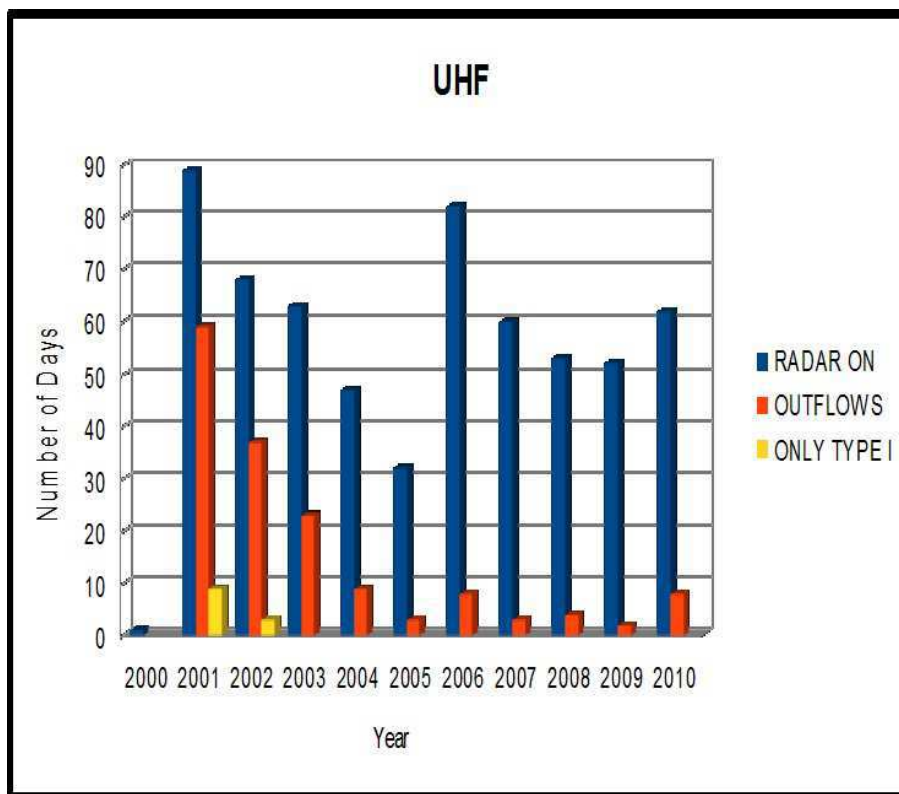
Figure 4.1.: Occurrences of ion outflows and type-I ion outflows detected with the UHF
radar.

We detected type-I ion outflows only in the years 2001 and 2002, which are the years with
the highest number of outflows identified (59 and 37, respectively). The reason may be
related to the fact that very few ion outflows were detected during the remaining years
(always less than 10) and no outflows were detected during the year 2000. We also notice
that the data were quite often too noisy and this could be one reason why we detected so
few outflows. The only exception is the year 2003, where a fairly high number of outflows
have been detected (23), but no type-I outflows were identified.

In Tab. 4.1 the type-I ion outflows detected and their characteristics are listed. In the first
column the date when each type-I ion outflow has been detected is reported.
In the second column it is shown in which category, either continuous or non-continuous,
each outflow has been included. Notice that all the type-I ion outflows detected are non-
continuous.
The time interval where each outflow occurs is reported in the third column. Notice that
the minimum time interval is one hour, which is the minimum data set which can be
downloaded from the Madrigal database. If for example an outflow occurred between
2250 UT and 2320 UT in the evening, the time interval reported in the table is 2200-
2400 UT. Notice that all the events detected occur during the evening or night hours, in
particular they occur between 1900-0200 UT.
The fourth column shows the altitude range of each experiment.
In the last column, a brief explanation of the behavior of the electron density is reported.
When "small particle precipitation" is reported, we detect slight enhancements in the

electron density below 200-300 km.

We also note that the general outflow occurrence seem to follow the sunspot numbers with the prolonged minimum in the years 2007-2009 (http://www.spaceweather.com).

Date (dd-mm-yyyy)	Type	Time (UT)	Experiment Altitude (km)	Electron Density
06-02-2001	non-continuous	2300-0000	100-700	low below 300 km (with gap)
07-02-2001	non-continuous	0000-0100	100-700	low below 300 km
13-02-2001	non-continuous	2100-2200	100-700	low below 250 km
14-02-2001	non-continuous	2100-2300	100-700	low below 300 km (with gap)
29-04-2001	non-continuous	0100-0200	100-700	low below 300 km (with gap)
08-07-2001	non-continuous	0000-0100	100-700	low below 300 km (with gap)
17-09-2001	non-continuous	2200-2300	100-700	low below 200 km
18-10-2001	non-continuous	1800-2000	100-700	low below 200 km
18-11-2001	non-continuous	2100-0000	100-700	low below 250 km
18-02-2002	non-continuous	2300-0000	100-700	small particle precipitation
20-02-2002	non-continuous	2000-2200	100-700	low below 200 km
19-11-2002	non-continuous	0100-0200	100-700	small particle precipitation

Table 4.1.: Characteristics of type-I ion outflows detected by the UHF radar.

Fig. 4.2 shows the temperature ratio T_e/T_i (upper panel), the ion velocity (middle panel) and the electron density (bottom panel) as a function of time and altitude for the UHF radar. The box identifies the outflow event. It is possible to see that when the outflow starts the temperature ratio is larger than one, when the velocity increases (it becomes red) the ratio becomes less than one and then it increases again to values larger than one.

In addition, it is possible to see in Fig. 4.2 an example of the "evident gap" in the electron density reported in Tab. 4.1.

4.1.2. VHF radar

We used experiments with the VHF radar pointing at: ~ 70 degrees, ~ 75 degrees or ~ 90 degrees.

The results are summarized in the histogram in Fig. 4.3. As we mentioned in sec. 4.1.1, the blue columns show the number of days where the radar was on (in this case the VHF), the red columns show the number of days where outflows have been detected and the yellow columns show the number of days where type-I ion outflows have been identified.
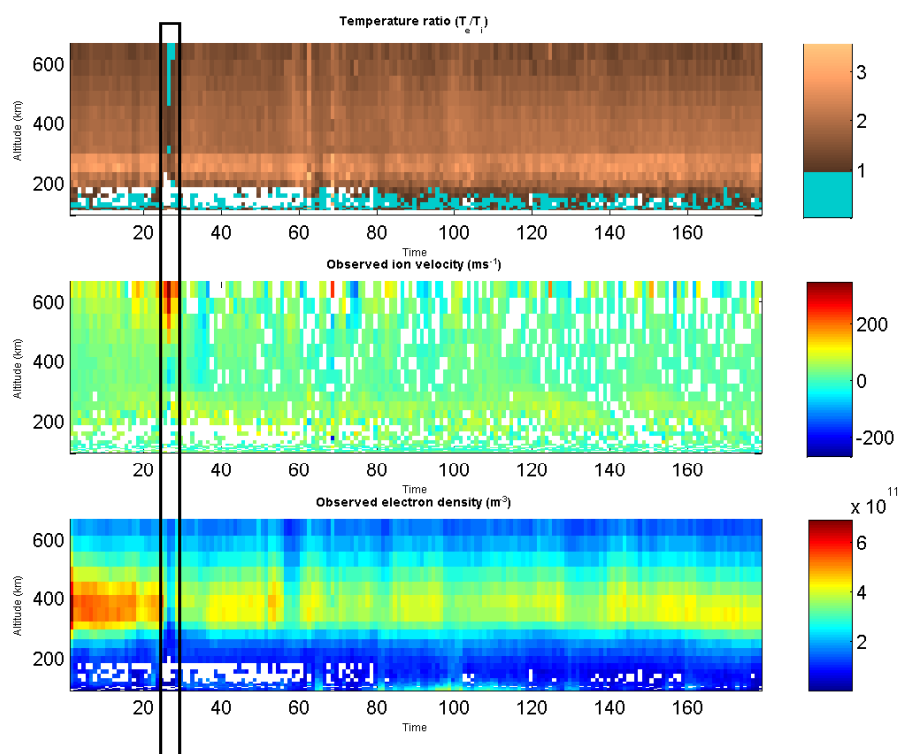
Figure 4.2.: In the first panel the temperature ratio T_e/T_i is plotted. The second panel shows the ion drift velocity (ms^{-1}). In the third panel the electron density (m^{-3}) is plotted. Data from the 8th of July 2001, UHF radar.

Notice that the number of days when the radar was on is fairly low. The highest number occurs in the year 2010 (29 days), followed by 2007 (17 days).

We detected type-I ion outflows during the years 2000, 2001, 2002, 2003, 2009 and 2010.

No data were available for the year 2005 and no outflows were detected during the years 2006 and 2008.
We also note here that in spite of the lack of observations, the general outflow occurrence seems to follow the sun spot cycle.

It is important to note that the 2 type-I outflows detected during the year 2003 have been classified as type-I only by the use of the colour plots because it was not possible to carry the analysis of the data and plot the temperature ratio. Our matlab program could not read the NCAR file with the parameters measured by the radar.

In Tab. 4.2 the characteristic of the detected type-I ion outflows are listed.

From the VHF data we detected both non-continuous and continuous outflows, but the only two continuous outflows identified are from two experiments with measurements from only high altitudes (400-2300 km).
We cannot say anything about the two outflows detected during the year 2003, because we could not plot the temperature ratio, as mentioned above.
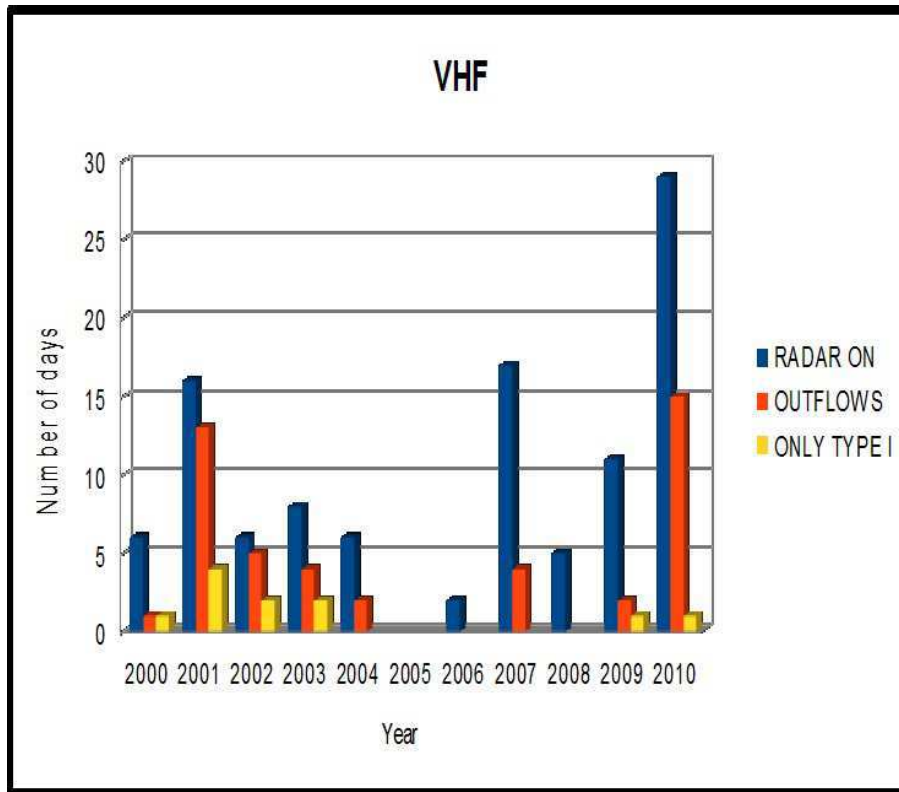
Figure 4.3.: Occurrences of ion outflows and type-I ion outflows detected with the VHF radar.

All the events occur in the time interval 1600-0600 UT. In this case, the electron density situation is more unclear because some of the experiments start from higher altitudes than usual, and so it was not possible to check the behavior of the electron density below 200-300 km, see Tab. 4.2.

4.1.3. ESR radar

We used experiments with the ESR radar pointing at: ~ 81 degrees or ~ 90 degrees.

The results are summarized in the histogram in Fig. 4.4. As we mentioned in the previous sections, the blue columns show the number of days where the radar was on (in this case the ESR), the red columns show the number of days where outflows have been detected and the yellow columns show the number of days where type-I ion outflows have been identified.

We detected type-I ion outflows during the years 2000, 2001, 2002, 2003, 2006 and 2007. It is important to point that one of the outflows detected during the year 2007 has been identified using only the colour plot (due to the same problem with the NCAR file as with the 2 outflows from 2003 in sec. 4.1.2).

We identified both non-continuous and continuous outflows. An example of continuous type-I ion outflow is given in Fig. 4.5. The events occur in the time interval 1800-0000

Date (dd-mm-yyyy)	Type	Time (UT)	Experiment Altitude (km)	Electron Density
08-11-2000	non-continuous	2100-2300	400-2300	
07-03-2001	non-continuous	0000-0100	400-2300	
18-09-2001	non-continuous	2200-0000	200-2000	low between 200 and 300 km
16-10-2001	1 continuous, 1 non-continuous	2200-0000	400-2300	
17-10-2001	non-continuous	0000-0300	400-2300	
07-10-2002	non-continuous	0200-0600	400-2300	
08-10-2002	1 continuous, others non-continuous	2200-2300	400-2300	
21-10-2003		1600-1700	100-1300	low below 300 km (with gap)
22-10-2003		0300-0500	100-1300	low below 300 km (with gap)
26-11-2009	non-continuous	1600-1800	100-600	small particle precipitation
13-04-2010	non-continuous	2200-2300	100-700	low below 300 km (with gap)

Table 4.2.: Characteristics of type-I ion outflows detected by the VHF radar.

UT and 0000-1100 UT. In Tab. 4.3 an overview of the characteristics of the outflows is given.

4.2. NEIALs and type-I outflows

To verify if NEIALs were present during type-I ion outflows we analyzed data using the real-time-graph (rtg) file of each experiment. The rtg file is a matlab script included in the data downloadable from the Madrigal database that allows plotting of the power spectrum and consequently identify NEIALs. In Fig. 4.6 a typical plot of NEIAL using the rtg file is shown as an example.

Unfortunately not all the experiments include the rtg file and sometimes it does not work properly, so we could not verify the presence of NEIALs for all the days when type-I ion
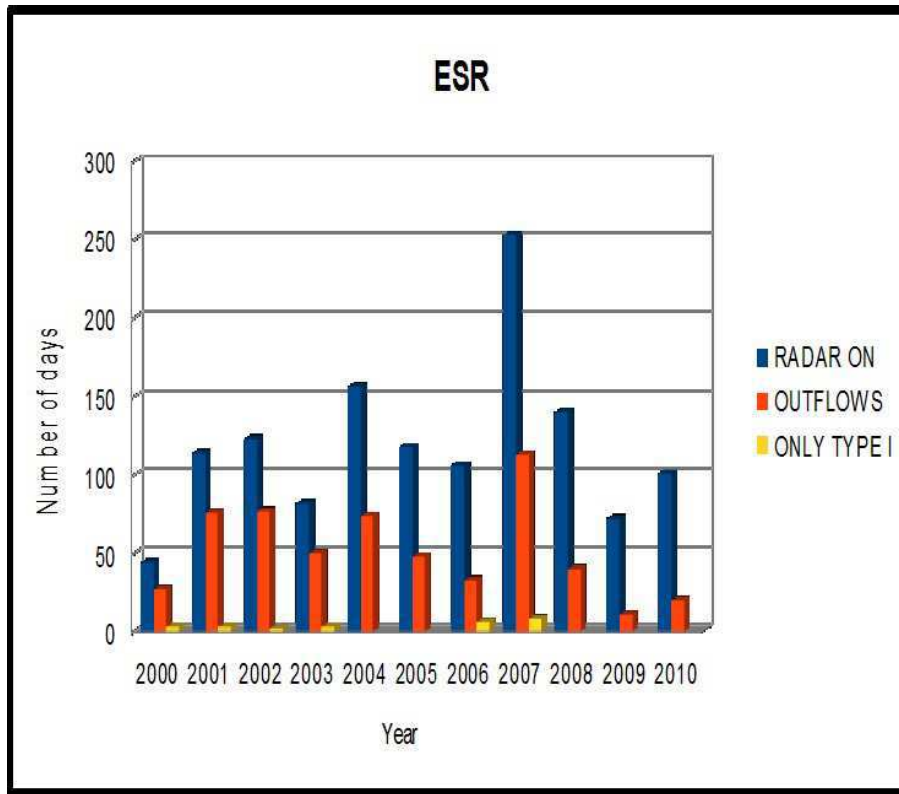
Figure 4.4.: Occurrences of ion outflows and type-I ion outflows detected with the ESR radar.

outflows have been detected.

4.2.1. UHF radar

All the days when type-I ion outflows were detected lacked the rtg file. As a consequence, it was not possible to verify the presence of NEIALs.

4.2.2. VHF radar

No rtg files were available for the years 2000, 2001 and 2002; but they were for the years 2003, 2009 and 2010.

The rtg files of the two outflows detected during the year 2003 did not work properly so we could not analyze them.

We analyzed data of the two days in 2009 and 2010 during the time interval when the type-I outflows was detected (see Tab. 4.2) and we did not find NEIALs.
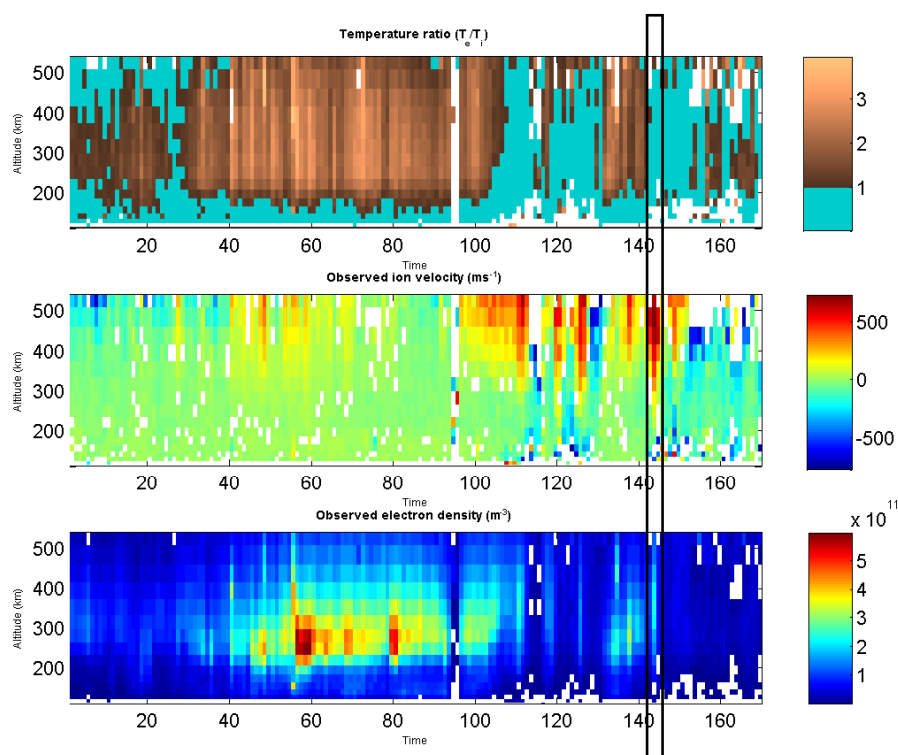
Figure 4.5.: In the first panel the temperature ratio T_e/T_i is plotted. The second panel shows the ion drift velocity (ms^{-1}). In the third panel the electron density (m^{-3}) is plotted. Data from the 23rd of January 2006, ESR radar.

4.2.3. ESR radar

No rtg files were available for the years 2000, 2001 and 2002; about the remaining years, the days when rtg files are available are listed below:

- 23-11-2003: the rtg file did not work properly so we could not check if NEIALs were present;

- 16-03-2006: we did not find NEIALs during the type-I outflow;

- 30-09-2006: we found NEIAL events during the type-I outflow;

- all the days of the year 2007 (see Tab. 4.3): for all of them the rtg file did not work properly so we could not check if NEIALs were present.

The NEIAL events detected during the type-I outflow of 30-09-2006   In Fig. 4.7 is shown the type-I ion outflow detected on 30-09-2006 with the ESR. This outflow was fairly strong, the ion drift velocity was larger than 1000 ms^{-1}. Furthermore, there are evident structures of enhancements in the electron density, which may be related to particle precipitation.

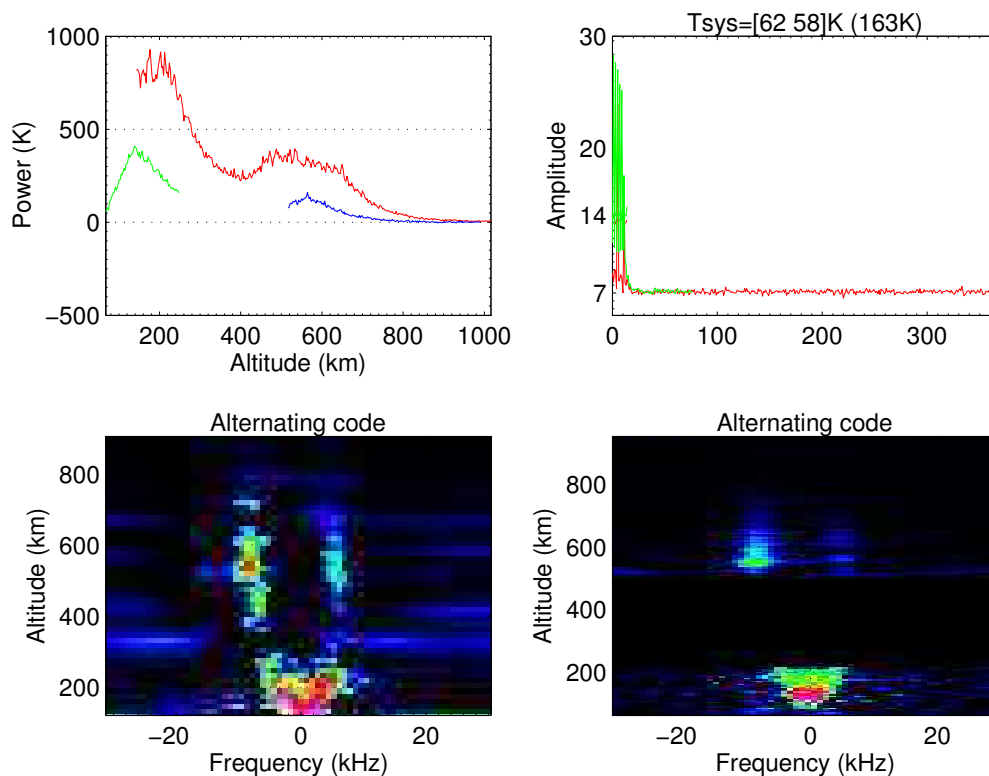steffel_fixed42m_1.40_CP 2005–03–31 0626:43 6.4s 991kW 182.1/81.6

Figure 4.6.: Typical plot of NEIAL using the rtg file is shown in the left bottom panel. Data from the ESR radar.

In Fig. 4.8 the outflow is shown more in detail, and we have marked the NEIAL events. The red vertical lines mark the dump when a NEIAL event was detected. Notice that most of them occur before the outflow event starts.

During the outflow, NEIAL events have been detected. These events are marked in the figure with the numbers 1 and 2, respectively.

Furthermore, the dumps before and after each NEIAL events have been marked with yellow vertical lines.

The event 1 corresponds to NEIALs detected in two successive dumps (the integration time was 5 seconds), at 10:08:14s and 10:08:19s. The event 2 marks NEIALs detected in two successive dumps at 10:42:34s and 10:42:39s. Each pair is embedded in one integration period of 30 seconds in the colour plot in Fig. 4.8. This is the reason why each pair has been marked with a single red vertical line (1 and 2 respectively).

Fig. 4.9 shows a detailed colour plot of the temperature ratio before and after NEIALs corresponding to number 1. The first panel shows the temperature ratio 10 dumps before the NEIALs, which occur in the dump number 154. The second panel shows the temperature ratio 10 dumps after NEIALs. The ratio is clearly less than 1 in the dumps before and after NEIALs occur.
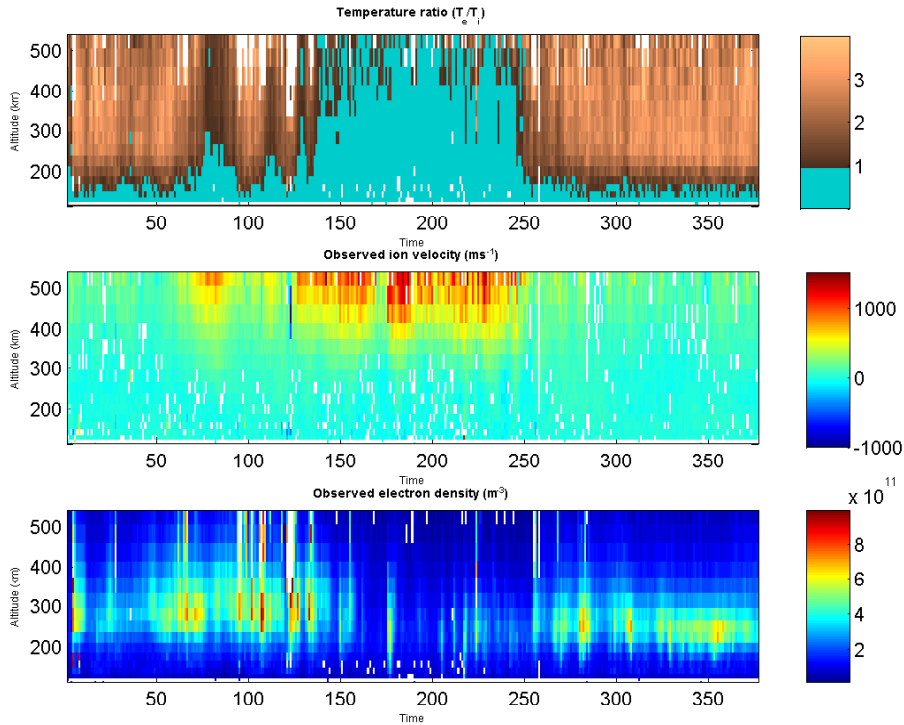
NEIALs detected at 10:08:14s are shown in Fig. 4.10.

Figure 4.7.: Type-I ion outflow detected the 30-09-2006.

In Fig.4.11 a detailed colour plot of the temperature ratio before and after NEIALs corresponding to number 2 is shown. The first panel shows the temperature ratio 10 dumps before NEIALs, which occur in the dump number 223. The second panel shows the temperature ratio 10 dumps after NEIALs. As it is shown in Fig.4.12, NEAILs start at $\sim$ 200 km. At those altitudes, the ratio is clearly less than 1 in the dumps before and after NEIALs occur.

NEIALs detected at 10:42:34s are shown in Fig.4.12.

We also found events which resemble NEIALs but they appear to be of lower intensity, we did not mark them in Fig.4.8.
This type of events have been reported in *Di Loreto* (2013). We detected this type of events both before and during the outflow, and an example is shown in Fig.4.13.

4.3. Flickering outflows

During the identification process of type-I ion outflows we noticed that there are events characterized by a different behavior of the temperature ratio T_e/T_i. These outflows can not be categorized neither as continuous nor as non-continuous type-I ion outflows, but they show a temperature ratio that changes in times and altitudes during the outflow fairly
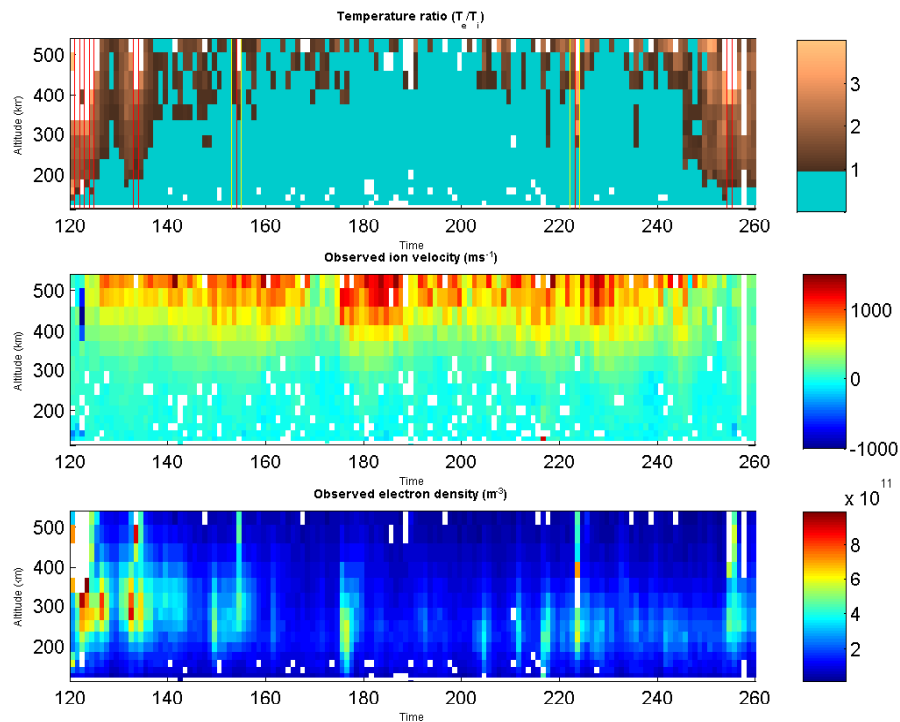
Figure 4.8.: Type-I ion outflow detected the 30-09-2006 with NEIAL events marked.

quickly. We will refer to these outflows as flickering outflows and we detected them with all the three radars. An example of flickering outflow detected with the VHF radar is given in Fig. 4.14.

It was not the aim of this thesis to count the days when these outflows were present, but similarly to the type-I ion outflows the few cases detected of flickering outflows seem characterized by a low electron density below 200-300 km, sometimes with a gap.
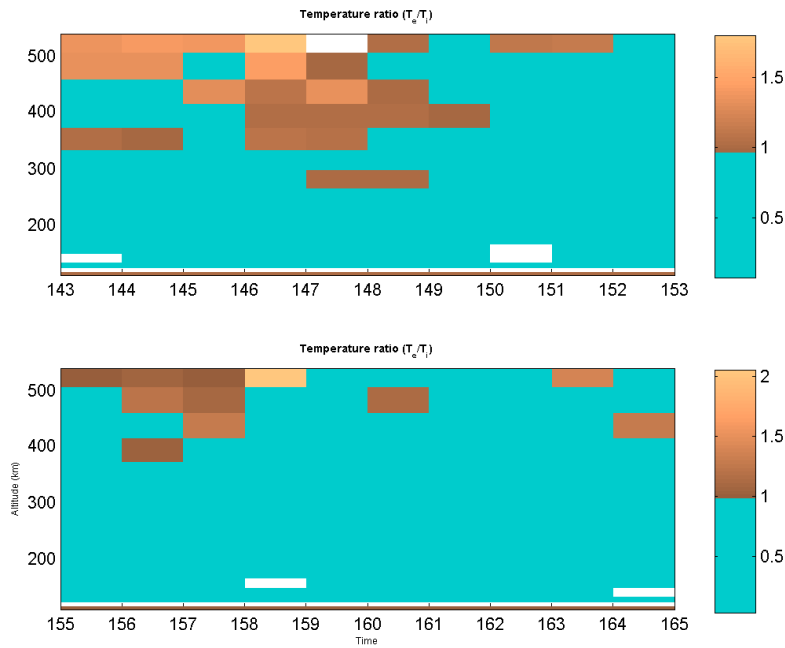
Figure 4.9.: Colour plot of the temperature ratio before and after the event 1.

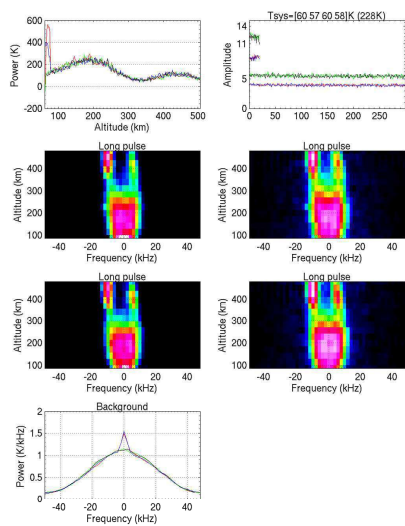**Figure 4.10.:** NEIAL detected at 10:08:14s during the type-I ion outflow detected on 30-09-2006.

Date (dd-mm-yyyy)	Type	Time (UT)	Experiment Altitude (km)	Electron Density
24-10-2000	non-continuous	2200-0000	100-800	low below 250 km
23-11-2000	non-continuous	0600-0800	100-800	low below 250 km
28-11-2000	non-continuous	2000-2200	100-800	low below 250 km
20-02-2001	non-continuous	0300-0500	100-800	low below 250 km
06-12-2001	non-continuous	0600-0800	100-800	low below 250 km
12-12-2001	non-continuous	0000-0200	100-800	low below 250 km
25-02-2002	non-continuous	0100-0300	100-800	low below 300 km
07-11-2002	non-continuous	2200-2300	100-800	low below 250 km
07-01-2003	non-continuous	0500-0700	100-800	low below 250 km
12-09-2003	non-continuous	2100-2200	100-800	low below 300 km (with gap)
23-11-2003	non-continuous	2100-2300	100-500	low below 250 km
23-01-2006	1 continuous, others non-continuous	0800-1100	100-550	low below 200 km
26-01-2006	non-continuous	0800-0900	100-700	low below 200 km (with gap)
16-03-2006	continuous	0000-0200	100-800	small particle precipitation
30-09-2006	non-continuous	0900-1100	100-600	small particle precipitation
23-11-2006	1 continuous, others non-continuous	0700-1100	100-800	low below 200 km (with gap), small part precipitation
24-11-2006	non-continuous	0400-0800	100-550	small particle precipitation
02-04-2007	continuous	0400-0500	100-500	small particle precipitation
15-04-2007	continuous	0000-0100	100-500	small particle precipitation
11-09-2007	continuous	2100-0000	100-500	low below 200 km (with gap)
29-09-2007	1 continuous, others non-continuous	0600-1000	100-500	low below 200 km (with gap), small particle precipitation
03-10-2007	non-continuous	0300-0500	100-500	small particle precipitation
21-10-2007	continuous	1800-1900	100-500	low below 200 km
25-10-2007	continuous	0100-0200	100-500	low below 200 km (with gap)
18-12-2007		0600-0700	100-500	low below 200 km

Table 4.3.: Characteristics of type-I ion outflows detected by the ESR radar.
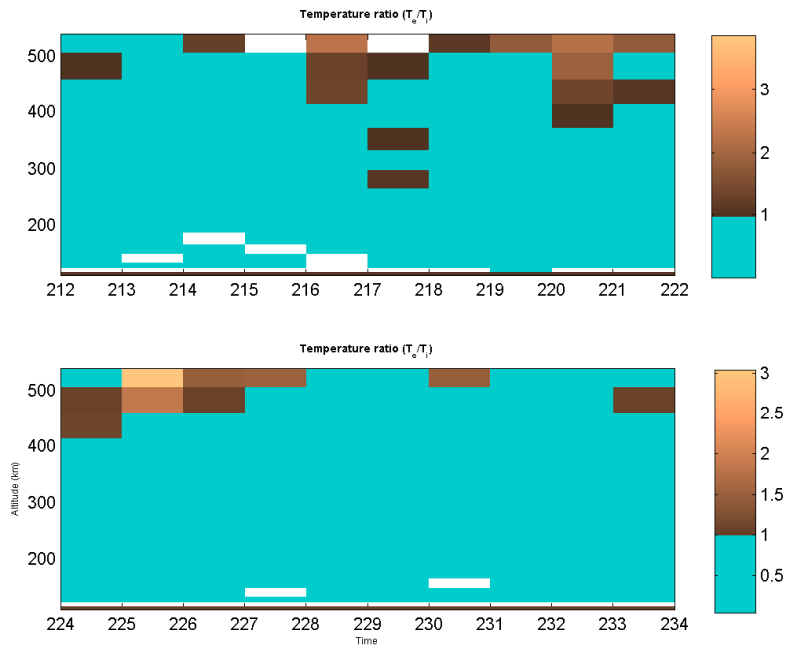
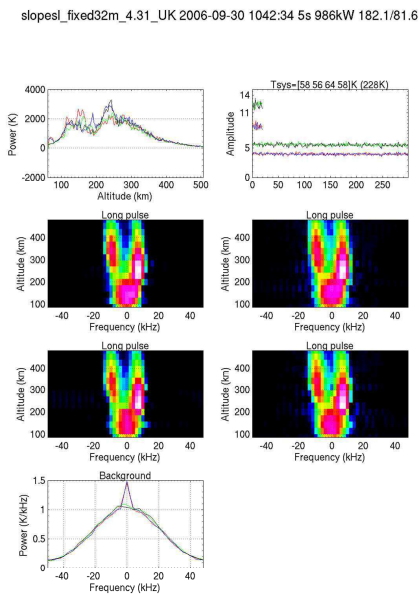**Figure 4.11.:** Colour plot of the temperature ratio before and after the event 2.

Figure 4.12.: NEIAL detected 10:42:34s during the type-I ion outflow detected on 30-09-2006.

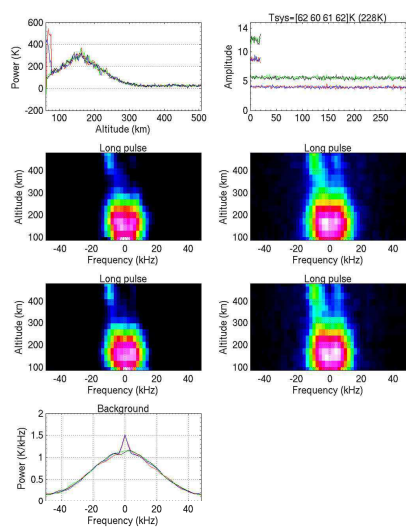slopesl_fixed32m_4.31_UK 2006-09-30 1043:54 5s 985kW 182.1/81.6

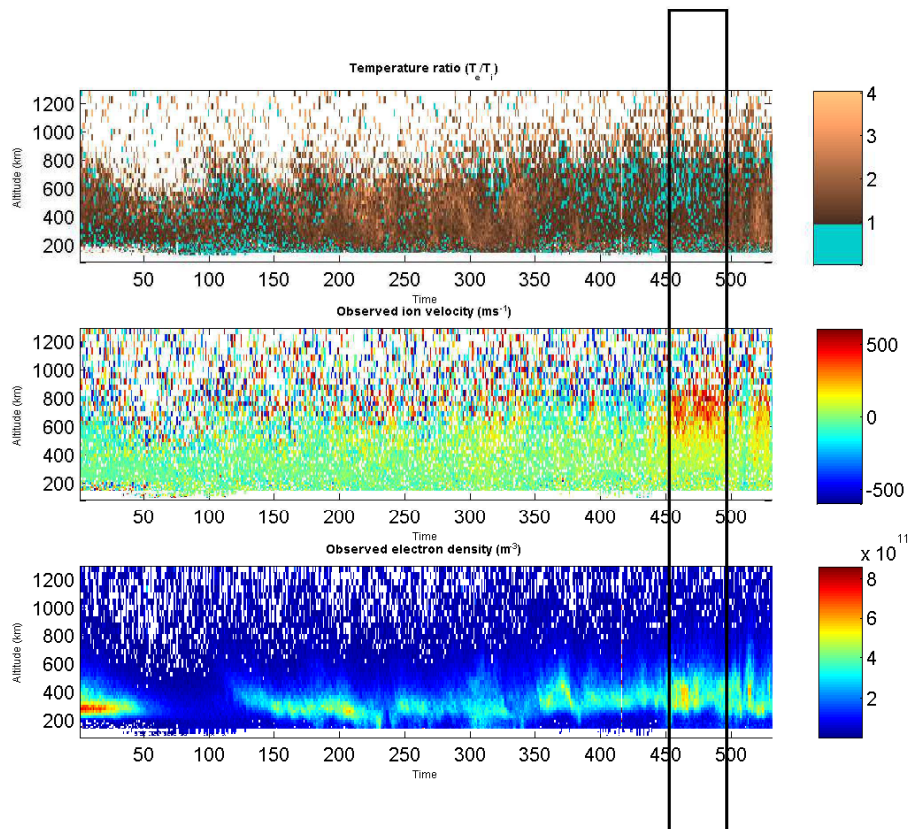**Figure 4.13.:** An example of event similar to NEIALs but of lower intensity detected on 30-09-2006.

Figure 4.14.: In the first panel the temperature ratio T_e/T_i is plotted. The second panel shows the ion drift velocity (ms^{-1}). In the third panel the electron density (m^{-3}) is plotted. Data from the 11th of December 2001, VHF radar.

5. Discussion

In this chapter a discussion about our results is given.

5.1. Discussion

We scanned the Madrigal database starting from the year 2000 until the year 2010. The type-I ion outflows detected have been divided into two categories: non-continuous and continuous. We also notice that there is a third situation which has not been reported in the literature before, which we call flickering outflows (see sec. 4.3).

We detected non-continuous outflows with the all the three radars, and we detected non-continuous outflows with the VHF radar and with the ESR radar. Notice that we identified only 2 continuous outflows with the VHF radar and they both occurred at very high altitudes. We could suggest that at the location of the ESR radar (Longyearbyen) and at higher altitudes there are different mechanisms that heat the ions than at lower altitudes and at the location of the UHF and VHF radars (Tromsø). At high altitudes wave activity has already been proposed as one possible cause of ion heating in the literature, we suggest that it may also be important in the ion heating at the location of the ESR at lower altitudes. At lower altitudes and at the location of the UHF and VHF, Joule heating could be the main mechanism which heats the ions.

In addition, all the outflows detected with the UHF and VHF radars occurred in the evening sector (see Tab. 4.1 and Tab. 4.2 respectively) while those detected with the ESR radar occurred both during the morning and evening sectors (see Tab. 4.3). The common feature that links the evening sector at the UHF and VHF location and the morning sector at the ESR location is particle precipitation. Moreover, all the events are characterized by either low electron densities below 200-300 km or very small amounts of hard particle precipitations. This may suggest that particle precipitations, especially soft particle precipitations, may be of relevance to trigger the type-I ion outflows.

Type-I ion outflows seem also to be fairly rare events, Tab. 5.1 shows the percentages of the type-I ion outflows occurrences for each radar (the percentages have been calculated dividing the number of days when outflows have been detected by the number of days when type-I outflows have been detected for each year and radar). Notice that the VHF radar displays the highest percentage each year.

When possible we analyzed data when type-I ion outflows occurred searching for the presence of NEIALs, and they have been found only during one type-I ion outflow event (30-09-2006, from the ESR). This outflow was fairly strong, it showed an ion drift velocity larger than 1000 ms^{-1} and it did present an enhancement in the electron density possibly

Year	UHF (%)	VHF (%)	ESR (%)
2000	no outflow detected	100	11.11
2001	15.25	30.77	3.95
2002	8.11	40	2.6
2003	0	50	6
2004	0	0	0
2005	0	no outflow detected	0
2006	0	no outflow detected	18.18
2007	0	0	7.08
2008	0	no outflow detected	0
2009	0	50	0
2010	0	6.67	0

Table 5.1.: Percentage of type-I ion outflows detected with the UHF, VHF and ESR radars.

related to particle precipitation. Notice that this was the only type-I ion outflow occurring in the morning sector which we could analyze.

The analysis from 30-09-2006 clearly shows that the temperature ratio T_e/T_i is less than 1 in both the dump before and the dump after NEIALs occurred. The incoherent scatter technique assumes a maxwellian distribution, and the distribution is not maxwellian when NEIALs occur. Therefor, the dump containing the NEIALs themselves have not been analyzed due to their turbulent nature. As a consequence, the ratio T_e/T_i in that dump can not be retrieved. There is a possibility that the ratio is larger than 1 during the dumps containing NEIALs but the analyzed parameters before and after suggest that T_e/T_i is less than 1 for a consecutive time period.

If this is the case we have to discuss the established theories for the generation mechanisms for NEIALs or look for other mechanisms which would fulfill the requirement of a temperature ratio less than 1. In fact, for the three theories proposed to generate NEIALs (see sec. 2.4) the authors assume a temperature ratio always larger than 3.

In addition, we want also to point out that it was not possible to analyze most of the type-I outflows detected. In Tab. 5.2 the percentages of type-I ion outflows analyzed are listed. Notice that most of the years present a percentage of analyzed type-I ion outflows equal to 0 and if we consider the total number of type-I ion outflows detected with the three radars, which is 48 (12 with the UHF, 11 with the VHF and 25 with the ESR), the percentage of analyzed type-I outflows in order to find NEIALs is 8.3%.

Further studies are required in order to be able to either find evident relations between type-I ion outflows and NEIALs which in this case we did not find because of the lack of a data set large enough, or to find out that NEIALs are extremely rare during type-I ion outflows.

Year	UHF (%)	VHF (%)	ESR (%)
2000	no type-I outflow detected	0	0
2001	0	0	0
2002	0	0	0
2003	no type-I outflow detected	0	0
2004	no type-I outflow detected	no type-I outflow detected	no type-I outflow detected
2005	no type-I outflow detected	no type-I outflow detected	no type-I outflow detected
2006	no type-I outflow detected	no type-I outflow detected	25
2007	no type-I outflow detected	no type-I outflow detected	0
2008	no type-I outflow detected	no type-I outflow detected	no type-I outflow detected
2009	no type-I outflow detected	100	no type-I outflow detected
2010	no type-I outflow detected	100	no type-I outflow detected

Table 5.2.: Percentage of analyzed type-I ion outflows detected with the UHF, VHF and ESR radars.

6. Conclusion and future work

In this chapter we present the conclusion of our work, followed by a description of possible future works.

6.1. Conclusion

Our study leads to the following conclusions:

- We detected 2 categories of type-I ion outflows: continuous ion outflows showing a temperature ratio T_e/T_i less than 1 at all altitudes and time and non-continuous ion outflows showing a temperature ratio T_e/T_i changing both in time and altitudes or changing either in time or altitudes.

- We detected non-continuous type-I ion outflows with the UHF, the VHF and the ESR radars. We detected continuous type-I ion outflows with both the VHF (only at high altitudes) and the ESR radars, suggesting different heating mechanisms.

- We detected type-I ion outflows in the evening sector with both the UHF and the VHF radars, and both in the evening sector and in the morning sector with the ESR radar, suggesting that particle precipitation may be relevant to trigger these outflows.

- We detected a third situation of ion outflows not reported in the literature before which we call flickering outflows showing a temperature ratio that changes at all times and altitudes fairly quickly.

- During one of the type-I ion outflows identified we detected NEIALs, suggesting that the proposed theories in the literature about the NEIAL generation mechanisms should be discussed in the future or that other mechanisms are needed to fulfill the requirement of a temperature ratio less than 1.

6.2. Future work

In this thesis we have used data from a period of 10 years using the UHF, VHF and ESR radars. We did not count the number of outflows (see sec. 3.2), because our results have been obtained only by the use of the colour plots available from the Madrigal database. We analyzed the data only when type-I ion outflows had been detected.

We chose to do so because writing a program and analyzing data over a temporal range of 10 years would have been a very time consuming work. But if such a program could

be written, one could set parameters to define outflows in terms of ion velocity, temporal and altitude ranges and temperature ratio T_e/T_i. In this way it would be possible to build a proper statistics about the different types of outflows.

Our study was also limited by the small number of data with a properly working rtg file available. As a consequence, if in the future more data can be analyzed to search for NEIALs during type-I ion outflows, it will be possible to investigate in detail the relation between them.

In addition we did not investigate the perpendicular ion temperature, this was beyond the time limit of this work. However, the use of experiments from the tristatic radar would give information about the perpendicular ion temperature and would give the possibility to check if an anisotropic ion temperature exists.

Acknowledgments

A. Matlab code

A.1. Code to get the colour plots

We wrote a matlab program to get the colour plots of the parameters obtained with the UHF, VHF and ESR radars. In particular we needed the colour plots of the temperature ratio T_e/T_i, the electron density and the ion drift velocity.

The first part of the matlab program to extract from the NCAR file the measured parameters is courtesy of *Di Loreto* (2013).
Notice that not all the NCAR files (which can be downloaded from the Madrigal website and contain the parameters measured by the radars) have the same structure. As a consequence we used three different versions of the program that follows, which is the most used one.

We added to our program four useful matlab functions which can be downloaded from the user community of the website Mathworks (http://www.mathworks.se).

The function "freezecolors" has been used to plot in the same colour plot subplots with different colourmap. The functions "cbfreeze" and "cbhandle" have been used to "freeze" the colourbar to the chosen colourmap. The function "vline" has been used to draw vertical lines in the subplot of the temperature ratio corresponding to NEIALs (we used this function only to analyze data from 30-09-2006 from the ESR radar).

```
clc;

%Automatically rename imported NCAR file to 'data'
%otherwise assume we have already loaded a mat data previously saved
%NOTE: in matlab usually one should not use this eval() trick...
ncarname = who('-regexp','NCAR*');
if ~isempty(ncarname)
    ncarname = ncarname{1};
    data = eval(ncarname);
end

%i=pulse number
i=1;
%Automatically check NCAR file for step and range
%range of altitudes (usually ipy=31,steffe=45,tau0=52)
%step is 526 or 736 for myguisdap(v8.7), 402 for eiscat madrigal
firstNaN=find(isnan(data(1:end,4)),1);
range=firstNaN-9;
st=find(~isnan(data(firstNaN:end,4)),1)+firstNaN-2;
if isempty(st)
    st=length(data);
```

```matlab
end
step=st*(i-1); %(step between successive times)*(pulse number)
start=5; %starting row for altitude and value


%columns of parameters from NCAR file
calt=1; %altitude
cvo=10; %ion velocity
cvoerr=15; %error on the ion velocity
ctr=8; %temperature ratio Te/Ti
ctrerr=13; %error on Te/Ti
cnel=6; %electron density Ne
cnelerr=11; %error on Ne
cno_nel=5; %[O+]/Ne
cti=7; %ion temperature Ti
ctierr=12; %error on Ti



%select time
starttime_h = data(start-4+step,7);
starttime_m = data(start-4+step,8);
endtime_h = data(start-4+step,11);
endtime_m = data(start-4+step,12);


%select value of altitude recursively
alt=zeros(range+1,length(data)/st);
for j=1:length(data)/st
    alt(:,j)=data(start+st*(j-1):start+range+st*(j-1),calt);
end
for j=1:length(data)/st
    alt(:,j)=alt(:,1);
end
%select raw where altitude >300 km
for j=1:range+1
    if alt(j,:)>300
        startalt=j;
        break;
    end
end


%select value of ion velocity recursively
vo=zeros(range+1,length(data)/st);
voerr=zeros(range+1,length(data)/st);
for j=1:length(data)/st
    vo(:,j)=data(start+st*(j-1):start+range+st*(j-1),cvo);
    voerr(:,j)=data(start+st*(j-1):start+range+st*(j-1),cvoerr);
end

%select value of Te/Ti recursively
tr=zeros(range+1,length(data)/st);
trerr=zeros(range+1,length(data)/st);
for j=1:length(data)/st
    tr(:,j)=data(start+st*(j-1):start+range+st*(j-1),ctr);
```

```matlab
    trerr(:,j)=data(start+st*(j-1):start+range+st*(j-1),ctrerr);
end

%select value of Ne and error on Ne recursively
nel=zeros(range+1,length(data)/st);
nelerr=zeros(range+1,length(data)/st);
for j=1:length(data)/st
    nel(:,j)=data(start+st*(j-1):start+range+st*(j-1),cnel);
    nelerr(:,j)=data(start+st*(j-1):start+range+st*(j-1),cnelerr);
end

%select value of [O+]/Ne recursively
no_nel=zeros(range+1,length(data)/st);
for j=1:length(data)/st
    no_nel(:,j)=data(start+st*(j-1):start+range+st*(j-1),cno_nel);
end

%select value of ion temperature recursively
ti=zeros(range+1,length(data)/st);
tierr=zeros(range+1,length(data)/st);
for j=1:length(data)/st
    ti(:,j)=data(start+st*(j-1):start+range+st*(j-1),cti);
    tierr(:,j)=data(start+st*(j-1):start+range+st*(j-1),ctierr);
end

%create array with hours of the experiment
time=zeros(1,length(data)/st);
for j=1:length(data)/st
    time(1,j)=data(1+st*(j-1),11);
end

%create array with date of the experiment
date=zeros(1,2);
date(1,1)=data(1,10);
date(1,2)=data(1,9);

%delete NaN/unreliable values
voerr(abs(vo)==32767)=NaN;
vo(abs(vo)==32767)=NaN;
vo(abs(voerr)==32767)=NaN;
voerr(abs(voerr)==32767)=NaN;
%when error=32766 we are using assumed data, so set error=0
voerr(voerr==-32766)=0;
%delete NaN/unreliable values
trerr(abs(tr)==32767)=NaN;
tr(abs(tr)==32767)=NaN;
tr(abs(trerr)==32767)=NaN;
trerr(abs(trerr)==32767)=NaN;
%when error=32766 we are using assumed data, so set error=0
trerr(trerr==-32766)=0;
%delete NaN/unreliable values
nelerr(abs(nel)==32767)=NaN;
nel(abs(nel)==32767)=NaN;
nel(abs(nelerr)==32767)=NaN;
nelerr(abs(nelerr)==32767)=NaN;
%when error=32766 we are using assumed data, so set error=0
```

```matlab
nelerr(nelerr==-32766)=0;
%delete NaN/unreliable values
no_nel(abs(no_nel)==32767)=NaN;
%delete NaN/unreliable values
tierr(abs(ti)==32767)=NaN;
ti(abs(ti)==32767)=NaN;
ti(abs(tierr)==32767)=NaN;
tierr(abs(tierr)==32767)=NaN;
%when error=32766 we are using assumed data, so set error=0
tierr(tierr==-32766)=0;

nel=(10.^(nel.*10^-3));
nelerr=(10.^(nelerr.*10^-3));
no_nel=no_nel.*10^-3;
tr=tr.*10^-3;
trerr=trerr.*10^-3;
%derive O+ density
no=zeros(range+1,length(data)/st);
noerr=zeros(range+1,length(data)/st);
no=no_nel.*nel;
noerr=no.*(sqrt((nelerr./nel).^2));
%derive electron temperature Te
te=zeros(range+1,length(data)/st);
te=tr.*ti;
%calculate error on te
terr=te.*(sqrt((trerr./tr).^2+(tierr./ti).^2));

%remove data with error > 50%
for col=1:length(data)/st
    for i=1:range+1
        if (voerr(i,col)/vo(i,col)) > 0.5
            vo(i,col)=NaN;
        end
        if (trerr(i,col)/tr(i,col)) > 0.5
            tr(i,col)=NaN;
        end
        if (nelerr(i,col)/nel(i,col)) > 0.5
            nel(i,col)=NaN;
        end
        if (tierr(i,col)/ti(i,col)) > 0.5
            ti(i,col)=NaN;
        end
        if (terr(i,col)/te(i,col)) > 0.5
            te(i,col)=NaN;
        end
        if (noerr(i,col)/no(i,col)) > 0.5
            no(i,col)=NaN;
        end
    end
end


%create array with numbers corresponding to hours of the experiment
t=1:length(data)/st;
```

A.1 Code to get the colour plots

```matlab
%PLOTS
figure(1)

%subplot of the temperature ratio
subplot(3,1,1)
tr(tr>4)=NaN;
tr(tr<0)=NaN;
newmap=copper;
%assign the color [0 0.8 0.8] to the portion of the plot where te/ti<1
nc=size(newmap,1);
zpos=floor(1/4.1*nc); %portion of the plot where te/ti<1 (must be ...
    adjusted)
i=1;
while i<=zpos
    newmap(i,:)=[0 0.8 0.8];
    i=i+1;
end
pcolor(t(:,120:260),alt(:,120:260),tr(:,120:260)); shading flat;
colormap(newmap); c1=colorbar;
vert=vline([t(1,120) t(1,121) t(1,122) t(1,123) t(1,124) t(1,125)...
    t(1,133) t(1,134) t(1,153) t(1,154) t(1,155) t(1,222) t(1,223)...
    t(1,224) t(1,254) t(1,255)],...
    {'r','r','r','r','r','r','r','r','y','r','y','y','r','y','r','r'});
freezeColors; %see www.mathworks.se for information
cbfreeze(c1); %see www.mathworks.se for information
title('Temperature ratio (T_e/T_i)','FontSize',7,'FontWeight','bold');
xlabel('Time','FontSize',6); ylabel('Altitude (km)','FontSize',6);

%subplot of the ion drift velocity
subplot(3,1,2)
vo(vo>15*10^2)=NaN;
vo(vo<-15*10^2)=NaN;
pcolor(t,alt,vo); shading flat; colormap(jet); c2=colorbar;
freezeColors;
cbfreeze(c2);
title('Observed ion velocity ...
    (ms^-^1)','FontSize',7,'FontWeight','bold');
xlabel('Time','FontSize',6); ylabel('Altitude (km)','FontSize',6);

%subplot of the electron density
subplot(3,1,3)
nel(nel>10*10^11)=NaN;
nel(nel<0.1*10^10)=NaN;
pcolor(t,alt,nel); shading flat; colormap(jet); c3=colorbar;
freezeColors;
cbfreeze(c3);
title('Observed electron density ...
    (m^-^3)','FontSize',7,'FontWeight','bold');
xlabel('Time','FontSize',6); ylabel('Altitude (km)','FontSize',6);

%save the figure with plots in eps format
saveas(1,'figp','epsc')
```

Bibliography

Amatucci, W. E., D. N. Walker, G. Ganguli, D. Duncan, J. A. Antoniades, J. H. Bowles, V. Gavrishchaka, and M. E. Koepke (1998), Velocity-shear-driven ion-cyclotron waves and associated transverse ion heating, *Journal of Geophysical Research: Space Physics*, *103*(A6), 11,711–11,724, doi:10.1029/98JA00659.

Banks, P., and G. Kockarts (1973), *Aeronomy*, no. v. 2 in Aeronomy, Academic Press.

Beynon, W. J. G., and P. J. S. Williams (1978), Incoherent scatter of radio waves from the ionosphere, *Reports on Progress in Physics*, *41*(6), 909–955.

Brekke, A. (2012), *Physics of the Upper Polar Atmosphere*, Springer.

Burchill, J. K., D. J. Knudsen, J. H. Clemmons, K. Oksavik, R. F. Pfaff, C. T. Steigies, A. W. Yau, and T. K. Yeoman (2010), Thermal ion upflow in the cusp ionosphere and its dependence on soft electron energy flux, *Journal of Geophysical Research: Space Physics*, *115*(A5), n/a–n/a, doi:10.1029/2009JA015006.

Di Loreto, M. (2013), On the relation between type-II ion outflow and naturally enhanced ion acoustic lines in the polar ionosphere, Master's thesis, University of Tromsø.

Fabry, C. (1928), Remarks concerning the scattering of light and electromagnetic waves by free electrons.

Forme, F. R. E. (1993), A new interpretation on the origin of enhanced ion acoustic fluctuations in the upper ionosphere, *Geophysical Research Letters*, *20*(21), 2347–2350, doi:10.1029/93GL02490.

Foster, J. C., C. del Pozo, K. Groves, and J.-P. St. Maurice (1988), Radar observations of the onset of current driven instabilities in the topside ionosphere, *Geophysical Research Letters*, *15*(2), 160–163, doi:10.1029/GL015i002p00160.

Ganguli, G., M. J. Keskinen, H. Romero, R. Heelis, T. Moore, and C. Pollock (1994), Coupling of microprocesses and macroprocesses due to velocity shear: An application to the low-altitude ionosphere, *Journal of Geophysical Research: Space Physics*, *99*(A5), 8873–8889, doi:10.1029/93JA03181.

Gordon, W. (1958), Incoherent scattering of radio waves by free electrons with applications to space exploration by radar, *Proceedings of the IRE*, *46*(11), 1824–1829, doi:10.1109/JRPROC.1958.286852.

Grydeland, T., C. La Hoz, T. Hagfors, E. M. Blixt, S. Saito, A. Strømme, and A. Brekke (2003), Interferometric observations of filamentary structures associated with plasma instability in the auroral ionosphere, *Geophysical Research Letters*, *30*(6), n/a–n/a, doi:10.1029/2002GL016362.

Hagfors, T. (1995), Plasma fluctuations excited by charged particle motion and their detection by weak scattering of radio waves.

Jones, G. O. L., P. J. S. Williams, K. J. Winser, M. Lockwood, and K. Suvanto (1988), Large plasma velocities along the magnetic field line in the auroral zone, *Nature*, *336*(6196), 231–232, doi:10.1038/336231a0.

Karttunen, H., P. KR÷GER, and H. Oja (2007), *Fundamental Astronomy*, Springer.

Kelley, M. (2009), *The Earth's Ionosphere: Plasma Physics & Electrodynamics*, International Geophysics, Elsevier Science.

Michell, R. G., K. A. Lynch, C. J. Heinselman, and H. C. Stenbaek-Nielsen (2009), High time resolution PFISR and optical observations of naturally enhanced ion acoustic lines, *Ann. Geophys.*, *27*(4), 1457–1467, doi:10.5194/angeo-27-1457-2009.

Nishida, A. (1966), Formation of plasmapause, or magnetospheric plasma knee, by the combined action of magnetospheric convection and plasma escape from the tail, *Journal of Geophysical Research*, *71*(23), 5669–5679, doi:10.1029/JZ071i023p05669.

Nygrén, T. (1996), *Introduction to Incoherent Scatter Measurements*, Invers Publications.

Rietveld, M. T., P. N. Collis, and J.-P. St.-Maurice (1991), Naturally enhanced ion acoustic waves in the auroral ionosphere observed with the EISCAT 933-MHz radar, *Journal of Geophysical Research: Space Physics*, *96*(A11), 19,291–19,305, doi:10.1029/91JA01188.

Schunk, R., and A. Nagy (2009), *Ionospheres: Physics, Plasma Physics, and Chemistry*, Cambridge Atmospheric and Space Science Series, Cambridge University Press.

Sedgemore-Schulthess, F., and J.-P. S. St. Maurice (2001), Naturally enhanced ion-acoustic spectra and their interpretation, *Surveys in Geophysics*, *22*(1), 55–92, doi:10.1023/A:1010691026863.

Wahlund, J.-E., F. R. E. Forme, H. J. Opgenoorth, M. a. L. Persson, E. V. Mishin, and A. S. Volokitin (1992a), Scattering of electromagnetic waves from a plasma: Enhanced ion acoustic fluctuations due to ion-ion two-stream instabilities, *Geophysical Research Letters*, *19*(19), 1919–1922, doi:10.1029/92GL02101.

Wahlund, J. E., H. J. Opgenoorth, I. Häggström, K. J. Winser, and G. O. L. Jones (1992b), EISCAT observations of topside ionospheric ion outflows during auroral activity: Revisited, *Journal of Geophysical Research: Space Physics*, *97*(A3), 3019–3037, doi:10.1029/91JA02438.

Wahlund, J.-E., et al. (1998), Broadband ELF plasma emission during auroral energization: 1. slow ion acoustic waves, *Journal of Geophysical Research: Space Physics*, *103*(A3), 4343–4375, doi:10.1029/97JA02008.

Nomenclature

BB-ELF   Broadband Extremely Low-Frequency

EISCAT   European Incoherent SCATter

ESR   EISCAT Svalbard Radar

IMF   Interplanetary Magnetic Field

NEIALs   Naturally enhanced ion acoustic lines

rtg   real-time-graph

UHF   Ultra High Frequency

UV   UltraViolet

VHF   Very High Frequency